

## **ABSTRACT**

MOERING, JORDAN, ALEXANDER. Unraveling Deformation Mechanisms in Gradient Structured Metals. (Under the direction of Yuntian Zhu and Suveen Mathaudhu).

Gradient structures have demonstrated high strength and high ductility, introducing new mechanisms to challenge conventional mechanics. This work develops a method for characterizing the shear strain in gradient structured steel and presents evidence of a texture gradient that develops in Surface Mechanical Attrition Treatment (SMAT). Mechanics underlying some theories of the strengthening mechanisms in gradient structured metals are introduced, followed by the fabrication and testing of gradient structured aluminum rod. The round geometry is intrinsically different from its flat counterparts, which leads to a multiaxial stress state evolving in tension. The aluminum exhibits strengthening beyond rule of mixtures, and texture evolution in the post-mortem sample indicates that out of plane stresses operate within the gradient. Finally, another gradient structured aluminum rod is shown to exhibit higher strength and higher elongation to failure in a variety of sample diameters and processing conditions. The GND density and microstructural evolution showed no significant changes during mechanical testing, and high resolution strain mapping was successfully completed within the core of the material. These discoveries and contributions to the field should help continue unraveling the deformation mechanisms of gradient structured metals.

© Copyright 2016 by Jordan Alexander Moering

All Rights Reserved

Unraveling Deformation Mechanisms in Gradient Structured Metals

by  
Jordan Alexander Moering

A dissertation submitted to the Graduate Faculty of  
North Carolina State University  
in partial fulfillment of the  
requirements for the Degree of  
Doctor of Philosophy

Material Science and Engineering

Raleigh, North Carolina

2016

APPROVED BY:

---

Yuntian Zhu  
Committee Chair

---

Suveen Mathaudhu

---

Carl Koch

---

Ronald Scattergood

## **DEDICATION**

This dissertation is dedicated to the countless family members, friends, advisers, colleagues, and mentors who have provided me the guidance, support, and direction needed for me to complete this work. When facing an apparent insurmountable challenge like the volume of work needed for a Ph.D., having support of a strong team behind you is truly invaluable.

I also want to dedicate this work specifically to my wife, Nicole. For putting up with long nights, low pay, and my endless frustration with grace beyond measure.

## **BIOGRAPHY**

I'm going to do my biography in first person voice. Growing up, I was always eager to learn about everything around me, and could often be found digging up rocks and playing outside. I was naturally inclined towards artistic endeavors and fully considered pursuing a degree in art or literature for almost my entire life. All this changed when as teenager, I built a 7 ton steel torsion catapult with my father that launched pumpkins over 3,000 feet at nearly the speed of sound. We were featured on the science channel and competed regularly at the World Championship Punkin Chunkin with our catapult, Roman Revenge. It was during these exciting competitions that I got bit by the engineering bug and decided to focus my efforts on a college degree in Material Science and Engineering.

Throughout undergrad however, I continued exploring my artistic talents and simultaneously rose to a leadership role at the student paper managing a staff of 20+ photographers. I had found that I enjoyed seamlessly filling the roles of an engineer, artist, leader, and scientist at the same time. I worked at several internships working with steel and heat treatments as well as making titanium billet for aerospace, energy, and medical device applications. Not only did I find the engineering and science fascinating at these internships, but thoroughly enjoyed working with customers, supervisors, and shop floor operators to get my research projects completed ahead of schedule.

After my work experience, I decided to enter graduate school, in large part due to the encouragement of mentors like Suveen Mathaudhu, Roger Russell, Robert Moering, and Yuntian Zhu. Recently, I've utilized my diverse interests and expertise in co-founding a

startup company, WarpSpec, Inc. that has quite sufficiently thrust me into the business world, where understanding science and physics isn't as important as being able to hold a conversation. For the past 9 months I've had 3 jobs to work, which has forced me to examine my research through a more streamlined, critical lens. I can't thank enough all of the friends, family, colleagues, mentors, and acquaintances who have helped catapult me through my graduate work. It's been a long ride, but I think I'm ready to close this chapter of the book, and begin a new adventure in an exciting career.

## **ACKNOWLEDGMENTS**

I would like to acknowledge all of my colleagues, collaborators, mentors, group members, and advisers who helped support this work. I would also like to acknowledge the Analytical Instrument Facility for the equipment used to acquire a large majority of the presented data.

## TABLE OF CONTENTS

<b>LIST OF FIGURES .....</b>	<b>viii</b>
<b>1 Overview .....</b>	<b>1</b>
1.1 Nanocrystalline Metals.....	1
1.2 Severe Plastic Deformation.....	3
1.3 Gradient Structures.....	6
1.3.1 Introduction.....	6
1.3.2 Multiaxial Stress State Evolution.....	7
1.3.3 Cascading Dislocation Model.....	9
1.3.4 Residual Stress Effect.....	11
1.4 Plasticity and Texture.....	14
1.4.1 Slip in Single Crystals.....	14
1.4.2 Slip in Polycrystalline Metals.....	16
1.4.3 Dislocation Type.....	17
1.4.4 Texture Interpretation.....	18
1.5 Motivation.....	19
<b>2 Synthesis and Characterization.....</b>	<b>21</b>
2.1 SPEX Milling of Flat Samples.....	21
2.1.1 Effect of Ball Size.....	23
2.1.2 Processing Time.....	26
2.2 SPEX Milling of Round Samples.....	27
2.3 Introduction to EBSD.....	29
2.4 Strain Analysis using High Resolution EBSD.....	30
<b>3 Flat Gradient Structures.....</b>	<b>34</b>
3.1 Introduction.....	34
3.2 Experimental Procedure.....	35
3.3 Strain Analysis.....	36
3.4 Microstructural Analysis.....	41
3.5 Texture Analysis.....	48
3.6 Conclusions.....	54
<b>4 Round Gradient Structures.....</b>	<b>55</b>

4.1	Introduction .....	55
4.2	Experimental Procedure .....	57
4.3	Tensile Properties .....	57
4.4	Relationship between Hardness and Yield Strength .....	59
4.5	Rule of Mixtures Prediction .....	61
4.6	Microstructural Analysis .....	62
4.7	Post-Mortem Analysis .....	65
4.8	Conclusions .....	67
<b>5</b>	<b>Strain Analysis in Gradient Structured Rod.....</b>	<b>69</b>
5.1	Introduction .....	69
5.2	Experimental Procedure .....	70
5.3	Tensile Results .....	73
5.4	GND Density Evolution .....	81
5.5	EBSD Strain Analysis .....	82
5.6	XRD Strain Analysis .....	85
5.7	Conclusions .....	88
<b>6</b>	<b>Conclusions and Future Work.....</b>	<b>90</b>
<b>7</b>	<b>REFERENCES.....</b>	<b>92</b>

## LIST OF FIGURES

Figure 1.1 Flow stress dependency on grain size, showing deviation from the ideal Hall-Petch relationship in the nanocrystalline regime (grain size < 100 nm).....	2
Figure 1.2 (a) Small balls used in the SMAT process are accelerated and impact the sample in random directions. (b) Subsequently, the repeated impacts induce severe plastic deformation at the surface of the sample. ....	4
Figure 1.3 Schematic showing arbitrary increases in strain and strain rate within gradient structures created by SMAT [10].....	5
Figure 1.4 (a) Gradient structured IF Steel shows an improvement of ~2.5x in yield strength without significant ductility loss while (b) gradient structured copper shows both higher strength and higher elongation to failure [14,16].....	7
Figure 1.5 Schematic exaggerating the non-uniform deformation arising from the mechanical mismatch of competing layers within the gradient structure. (a) elastic deformation causes no stress gradients, (b) at low strains the interior will begin plastic deformation until (c) necking. ....	8
Figure 1.6 Strain induced grain growth and corresponding softening which accounts for extraordinary strengthening observed in gradient structured nanocrystalline copper [14,22].	11
Figure 1.7 Finite Element Modeling of the evolution of residual stresses induced by SMAT at various tensile loads before and after the onset of plastic deformation [30]. ....	13

Figure 1.8 Cartoon showing the relationship between an applied stress, $\sigma_u$ , and its angles relative to the slip plane and direction. ....	15
Figure 2.1 (a) Cross sectional FIB image of 99.9% Iron SMATed for 15 mins at 20kHz showing very little grain refinement at the surface. (b) TEM confirms that the grain size is not significantly reduced at this condition. ....	22
Figure 2.2 (a) the SPEX vial typically used for high energy ball milling of powders. (b) Replacing the lid with a plate of a material naturally creates SMAT microstructures. ....	23
Figure 2.3 (a) Low carbon steel SMATed for 60 minutes using (a) 1/8" stainless steel balls and (b) 1/2" stainless steel balls. ....	24
Figure 2.4 Higher magnification ion channeling contrast of the very top SMAT surface processed for 60 minutes with (a) 1/8" stainless steel balls and (b) 1/2" stainless steel balls. ....	25
Figure 2.5 Low carbon steel SMATed with 1/2" stainless steel balls for (a) 30 minutes (b) 120 minutes. ....	26
Figure 2.6 Higher magnification ion channeling contrast of the very top SMAT surface of a low carbon steel processed with 1/2" stainless steel balls for (a) 30 minutes and (b) 120 minutes. ....	27

Figure 2.7 (a) A custom SPEX vial used to process round samples. (b) An aluminum rod after SMAT processing in the vial for 5 minutes..... 28

Figure 2.8 Kikuchi patterns can be rotated or skewed in the presence of elastic strain, schematically shown here with a perfect lattice (black) overlaid onto a distorted lattice (red) [56]..... 31

Figure 2.9 When an incident beam interacts with a dislocated crystal, the locally strained region around the dislocation core will produce slightly different Kikuchi patterns, shown here. This effect is very pronounced over regions with high dislocation density, like a grain boundary or slip band, causing poor pattern quality [56]. ..... 32

Figure 3.1 Grid overlay used to partition the SEM cross section of the SMAT microstructure for shear strain analysis. Note the surface is tilted in order to align with the grid and collect accurate measurements. .... 37

Figure 3.2 (a) An SEM image of the as-received SMAT surface. The inset shows how the slope of the cementite bands was measured in order to calculate shear strain  $\gamma$ . (b) The resulting data calculated at various depths showing a clear exponential increase in shear strain approaching the surface of the SMAT gradient [86]. ..... 39

Figure 3.3 SEM cross sectional images of low carbon steel processed with 1/2” balls for (left) 30, (middle) 60, and (right) 120 minutes. .... 40

- Figure 3.4 Shear strain estimates collected from the grid overlay method outlined previously. Shear strain evolves exponentially approaching the surface, shown here plotted on a log scale..... 40
- Figure 3.5 (a) A cross sectional FIB image of the SMAT gradient extending to depths greater than 500  $\mu\text{m}$ , (b) the strong linear dependence of microhardness on shear strain, (c) the dependence of grain size on shear strain, and (d) the microhardness approximately follows the Hall–Petch relationship [86]. ..... 42
- Figure 3.6(a) high magnification ion channeling contrast image of the surface, where no  $\text{Fe}_3\text{C}$  is observable. (b) An image of the same sample 100  $\mu\text{m}$  below the surface showing regions of elongated and fragmented  $\text{Fe}_3\text{C}$ ..... 44
- Figure 3.7 (a) Bright field and (b) corresponding dark field TEM image of the top surface. Nanocrystalline grains <10nm in diameter are intermixed with 100 nm diameter  $\alpha$ -iron grains. It is also possible to discern several thin, elongated  $\text{Fe}_3\text{C}$  grains..... 45
- Figure 3.8(a) A representative image of the top surface shows regions with both nanocrystalline (<100 nm) grains and coarse grains intermixed. (b) High resolution TEM of the nanocrystalline region shows a single grain ~10 nm in diameter. This microstructure has been reported in steels subject to high shear strains and indicates partial decomposition of  $\text{Fe}_3\text{C}$ . (c) Grain size distribution at the top surface [86]. ..... 47

Figure 3.9 EBSD map of the top 60  $\mu\text{m}$  of the SMAT surface. Coloring schemes represent the orientation relative to the x, y, and z directions, for figures a, c, and e respectively, where the x direction is defined as the normal to the SMAT surface. (b, d, f) Coloring based on the value of each Euler angle within the SMAT surface. .... 49

Figure 3.10 Development of microstructure and texture at varying depths from the surface. The percentage of grains indexed normal to the SMAT surface were calculated from EBSD maps and show the relative frequency of the  $\{1\ 1\ 1\}$ ,  $\{1\ 1\ 0\}$  and planes in  $\alpha$ -iron at various depths. Grain boundary maps indicate high angle ( $>15^\circ$ ) grain boundaries in green, low angle ( $2^\circ$ ) boundaries in black. Pole figures are projected normal to the SMAT surface, indicating a strong  $\{1\ 1\ 0\}$ // SMAT surface texture developed in the top 50  $\mu\text{m}$  [86]. .... 52

Figure 4.1 (a) EBSD map of the O tempered aluminum and (b) after SMAT processing. (c) Microhardness profile at various depths and (d) Tensile test results of the SMAT and as-annealed samples with arrow indicating the rule of mixtures prediction of yield strength. (e) Color coded hardness map showing depth of the gradient to scale. .... 58

Figure 4.2 (a) Literature survey of hardness and yield strength results reported for low alloy aluminum. (b) Cartoon showing relationship between tensile properties and hardness for steels. .... 60

Figure 4.3 (a) Convention used for axis of the round SMAT sample along the surface normal (R), tensile direction (Z), and radial direction ( $\theta$ ). (b) Grain size gradient. (c and d) EBSD map of the SMAT sample projected along Z and grain boundary map, respectively. For the grain boundary maps, red lines indicate misorientation of  $>10^\circ$  and the black lines indicate misorientations  $>2^\circ$ . (e and f) High resolution EBSD map of the very top surface layer showing numerous subgrain boundaries when projected along Z and its grain boundary map, respectively. .... 63

Figure 4.4 (a) Z projection EBSD map of the uniformly elongated “as annealed” sample after tensile testing and corresponding pole figures showing (b) Symmetric smearing of  $\{110\}$  about the tensile (Z) axis and c)  $\theta$  axis projection. e) Z projection EBSD map of the uniformly elongated SMAT sample after tensile testing and corresponding pole figures projected along c) the Z axis and d) the  $\theta$  axis. There is a clear symmetry that develops along the  $\theta$  axis in the post mortem SMAT sample not present conventional samples. .... 66

Figure 5.1 (a,b)  $\theta$  and Z projection IPF maps, as defined by (c) of the as-annealed interior in the 5005 rod. (d) Z projected pole figure of the as-annealed 5005 rod showing a strong recrystallized wire texture. .... 72

Figure 5.2 EBSD map of the 6mm rod sample SMATed for 5 minutes (a-c) and for 15 minutes (d-f). (a,d) Grain boundary maps showing subgrain boundaries ( $>2^\circ$ ), low angle GB ( $>10^\circ$ ), and high angle GB ( $>15^\circ$ ). (b-e) the  $\theta$  projection IPF coloring and (c-f) the Z projection ..... 73

Figure 5.3 Engineering stress-strain curve plotted for the 4, 5, and 6 mm SMAT samples processed for 5 minutes compared to the O tempered state.....	74
Figure 5.4 Engineering stress-strain curve plotted for the 4, 5, and 6 mm SMAT samples processed for 15 minutes compared to the o tempered state. ....	75
Figure 5.5 Average yield strength for each diameter and processing condition.....	75
Figure 5.6 Average ultimate tensile strength for each diameter and processing condition. ...	76
Figure 5.7 Average uniform elongation for each diameter and processing condition.....	76
Figure 5.8 Tensile test and corresponding EBSD maps of 6mm samples SMATed for 5 minutes unloaded at various strains where the red curve is the gradient structure and the blue curve represents the o tempered tensile results. Grain boundary maps are colored black for subgrain boundaries ( $>2^\circ$ ), red for low angle grain boundaries ( $>10^\circ$ ), and green for high angle grain boundaries ( $>15^\circ$ ).....	78
Figure 5.9 Microhardness testing of the gradient structure showing profiles at various strains. Inset shows gradient hardness and volume fraction to scale. ....	80
Figure 5.10 Misorientation plots for 6mm samples unloaded at various strains. The plot shows an initial reduction in GND density which then rises with increased tensile strain. ...	82

Figure 5.11 (a) Full resolution Kikuchi pattern collected 50  $\mu\text{m}$  below the as SMAT surface showing clear evidence of plastic deformation relative to the same Kikuchi orientation collected (b) in the undeformed core. .... 83

Figure 5.12 Partial reconstruction of the strain tensor using collected Kikuchi patterns in the undeformed matrix of the SMAT sample. .... 84

Figure 5.13 XRD Analysis of 5 minutes SMAT and O-tempered 6mm rod. The peak shifts correspond to lattice strain which indicates residual compression at the surface of the SMAT sample. The relative intensity variations arise from the texture differences in the two samples. .... 87

## 1 Overview

### 1.1 Nanocrystalline Metals

Ever since the discovery of nanocrystalline metals in the late 1980s, investigating the mechanical properties and corresponding deformation mechanism(s) has led to a new approaches to create strong, lightweight, and ductile metals which was previously thought to be impossible [1]. As is often the case at extremely small length scales, nanocrystalline metals (grain sizes less than 100 nm) exhibit a wide variety of sometimes counter-intuitive properties which the structural metallurgist seeks to exploit in developing new metals for future applications. **Because one of the main objectives of a structural metallurgist is to create strong and ductile materials, the enhanced mechanical properties of nanocrystalline metals are of immediate interest.** The unique properties of these materials arise due to the length scales over which conventional deformation mechanisms operate. The nanocrystalline phase is fundamentally different from conventional, coarse grained metals due to the extraordinarily high volume fraction of grain boundaries. In general, plastic deformation in metals accumulates via dislocation interaction and annihilation and usually smaller grain sizes produce strong metals via Hall-Petch strengthening [2,3]. This mechanism is derived from the stress developed by dislocation pileup along grain boundaries that reduces plastic flow proportionally with the degree of grain refinement. This relationship means that smaller grain sizes often lead to greatly reduced ductility, as the crystallites within the sample exhibit little to no strain hardening. However, the Hall-Petch relationship has been experimentally disproven in the nanocrystalline and ultrafine grained regime, as grain

boundary rotation and sliding, deformation twinning, grain boundary emission of dislocations, and other strain accumulation schemes begin operating, most of which are poorly understood [4,5].

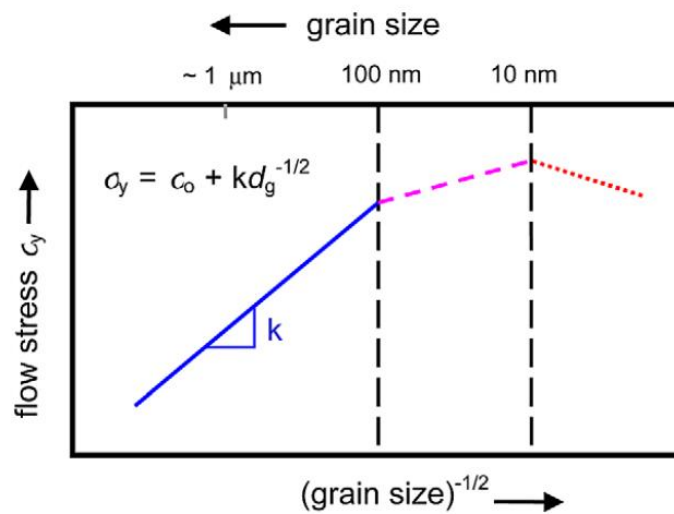


Figure 1.1 Flow stress dependency on grain size, showing deviation from the ideal Hall-Petch relationship in the nanocrystalline regime (grain size < 100 nm).

Therefore, opportunity exists to utilize the unique properties of nanocrystalline metals to improve both strength and ductility simultaneously [6]. One of the most well-known examples of this paradoxical improvement of mechanical performance is in nanocrystalline copper where the reduced grain size causes new deformation mechanisms to operate. Chiefly, deformation twinning is enhanced, causing improvement in both strength and ductility at the same time [7].

## 1.2 Severe Plastic Deformation

There are a wide variety of synthesis techniques that can be used to create nanocrystalline metals. Severe Plastic Deformation (SPD) is the name given to procedures by which coarse grained materials are repeatedly strained by a variety of techniques to produce ultrafine grained (UFG), nanocrystalline, or amorphous materials [8,9]. This class of procedures includes High Pressure Torsion (HPT), Ball Milling, Accumulative Roll Bonding (ARB), Equal Channel Angular Extrusion (ECAE), and Surface Mechanical Attrition Treatment (SMAT) among others. Although the techniques differ, the general grain refinement process in three stages. First, dislocations begin accumulating by becoming entangled with other dislocations formed within a grain. These tangled dislocations gradually form dense walls, or dislocation “cells” that extend from one side of a grain to another. The second step in the refinement process occurs when the dislocation cells become more refined subgrain boundaries, where  $\sim 2$  degrees of crystallographic misorientation is found across the subgrain interface. The last step in the nanocrystallization process occurs when the subgrain boundaries form low angle (10 degrees) grain boundaries. Additional strain accumulates along the grain boundaries to form more regular high angle (15 degrees) grain boundaries. This last step leaves the material in a nanocrystalline state with grains more or less free from internal strain as the energy requirement to store dislocation within the grain becomes prohibitively high. These steps are, however, a broad generalization of the nanocrystallization process. Variables such as the stacking fault energy, alloy composition, and numerous other factors affect the thermodynamics and kinetics of the refinement and

recovery processes that must be balanced to form a nanocrystalline phase [4]. An exhaustive list of factors affecting the degree and effectiveness of grain refinement will not be given here, but relevant factors will be discussed in later sections as it pertains to specific materials. However, it is sufficient to say that although SPD techniques themselves differ, they all confine the samples while inducing plastic deformation, which causes enormous dislocation accumulation within the grains of the metals.

Of the aforementioned techniques, SMAT is industrially scalable, effective in many metals, involves simple laboratory equipment, and has been widely studied. The technique shares many similarities with conventional shot peening, but larger balls, higher impact energies, and longer processing times are typically used [10–14].

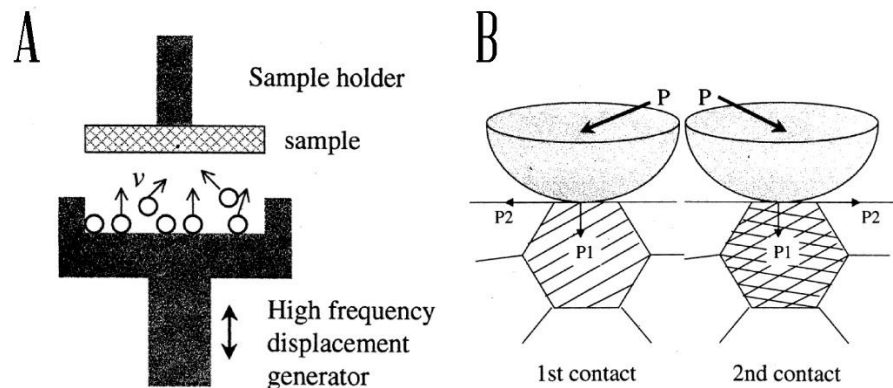


Figure 1.2 (a) Small balls used in the SMAT process are accelerated and impact the sample in random directions. (b) Subsequently, the repeated impacts induce severe plastic deformation at the surface of the sample.

In essence, the SMAT process involves repeatedly impacting the surface of a metal in a randomized fashion, which causes the surface to accumulate enormous dislocations. The end result is that the process creates a nanostructured surface that gradually transitions to the coarse grained, undeformed matrix. The degree of grain refinement can be quite pronounced, often to grain sizes  $<10$  nm, or even to the amorphous regime. The depth of this nanostructured layer often extends to depths of 50 micrometers, although this value varies widely with different processing conditions.

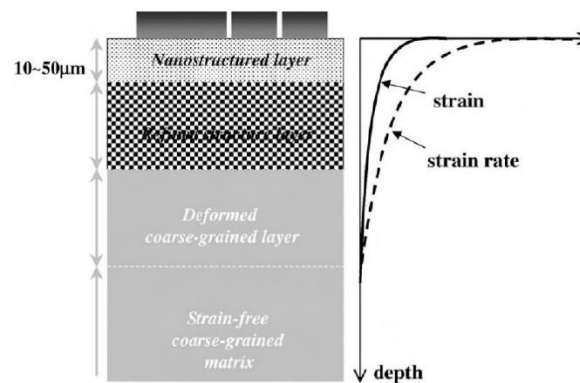


Figure 1.3 Schematic showing arbitrary increases in strain and strain rate within gradient structures created by SMAT [10].

However, in all cases the SMAT process allows a unique approach to study a single sample that possess many different grain sizes and degrees of accumulated strain. Unfortunately, much of the previous work sums to a qualitative understanding of how the SMAT process affects materials. This makes it very difficult to compare the microstructural

and mechanical properties of SMATed materials to other SPD literature. **As a result, quantitatively characterizing the effect of SMAT on the microstructure and mechanical properties along the gradient is of immediate scientific interest.** Finally, the SMAT process creates a unique “gradient structure”, whose global mechanical performance provides exciting avenues for improved strength and ductility.

### 1.3 Gradient Structures

#### *1.3.1 Introduction*

As we have seen, the nanocrystalline regime offers many unexpected deformation mechanisms that are intrinsically different from their coarse grained counterparts [14–22]. This mismatch of mechanical properties presents the opportunity to develop composite metallic systems where synergetic interactions may be exploited. For example, in carbon fiber composites, the high strength carbon fiber is embedded in a more ductile epoxy resin which can be optimized to create a strong, tough material for structural applications. However, unlike traditional composites, the gradient structured metals possess no sharp interfaces, which is one of the major weaknesses of composites. This is because in gradient structures, the ultra hard nanocrystalline region is completely coherent, via gradual microstructure variation, with the coarse grained region. As a result, the competing deformation mechanisms are forced to interact and compete during loading of the composite gradient structured metal. Due to this complex interaction, several theories have been proposed to explain the mechanics governing deformation of gradient structures.

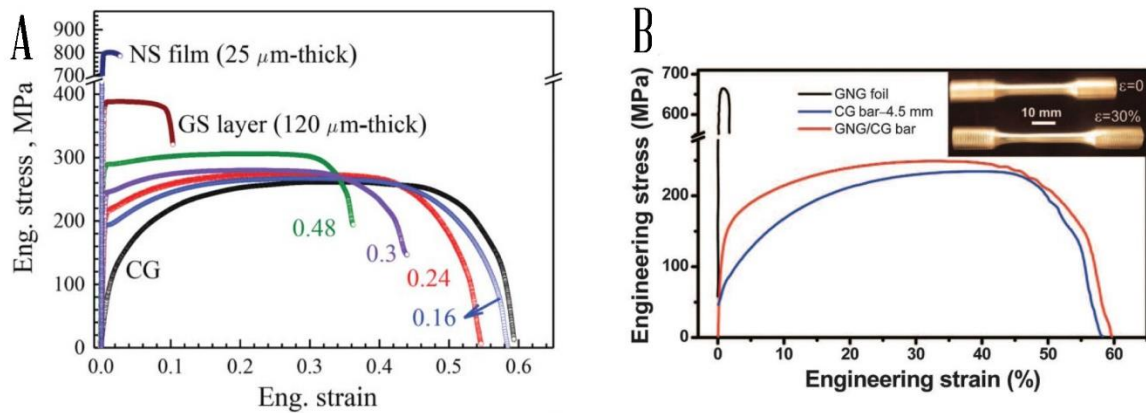


Figure 1.4 (a) Gradient structured IF Steel shows an improvement of  $\sim 2.5x$  in yield strength without significant ductility loss while (b) gradient structured copper shows both higher strength and higher elongation to failure [14,16].

### 1.3.2 Multiaxial Stress State Evolution

One theory that explains high strength and high ductility is the development of a multiaxial stress state that develops during tensile testing of a gradient structure. This multiaxial stress state is theorized to create more geometrically necessary dislocations, which thereby enhance strain hardening within the gradient [15,16]. When a gradient structure is at low strains of a uniaxial tensile test, both the coarse grained interior and nanocrystalline surface should be in the elastic region of their respective stress strain curves. Therefore, the entire gradient deforms in the same manner. However, above a certain strain threshold, the coarse grained interior will experience a stress greater than its respective yield stress, while the surface, by virtue of its high strength, will continue deforming elastically. Therefore, two competing deformation mechanisms are at hand within the gradient itself. The interior region

will attempt to contract, which puts the surface into compression, necessarily creating a multiaxial stress state within the gradient. At very high strains another mismatch occurs along the gradient as necking will begin in the surface layer, while the interior layer has not reached necking strains. Now the multiaxial stress will be reversed with the receding surface layer being balanced by the stable plastic core.

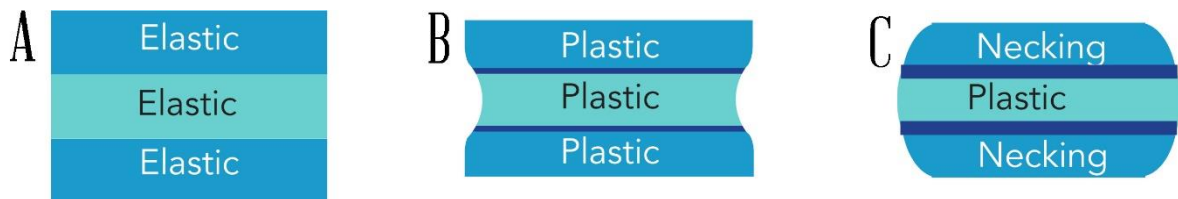


Figure 1.5 Schematic exaggerating the non-uniform deformation arising from the mechanical mismatch of competing layers within the gradient structure. (a) elastic deformation causes no stress gradients, (b) at low strains the interior will begin plastic deformation until (c) necking.

The net result of this mechanical mismatch within the gradient causes multiaxial stress states to develop in uniaxial tension which can develop unexpected tensile properties. The out of plane stress evolution has mainly been studied in flat samples, though early work on plasticity of composite metals suggested similar multiaxial stresses would develop in round samples [23]. Unfortunately, the interaction of the nanocrystalline regime and coarse grained interior under loading has not been systematically investigated, and is very poorly understood. There has been some evidence in flat samples to support this theory, since post-mortem analysis of the flat gradient sample showed dilation across the gradient not present in

the coarse grained counterpart [15,16]. Finite Element Analysis of a gradient structure showed very similar results, with a multiaxial stress gradient developing during tension [24]. Other than these observations, very little experimental evidence has been presented to explain the mechanical behavior and deformation mechanisms within the gradient layer.

### *1.3.3 Cascading Dislocation Model*

While the previous studies examined the interaction and competing deformation mechanism between different layers within the gradient, another theory suggests that plastic deformation causes plastic deformation to begin in the coarse grained core and then expand outwards, suppressing strain localization and enhancing dislocation accumulation within the gradient [21]. This mechanism suggests that initially, plastic deformation begins in the interior, where the onset of plastic deformation begins at low tensile strains. At higher strains, the plastic deformation front begins moving outward through the gradient, inducing cold work and hardening as it progresses. Because the strain accumulation is occurring within the coarse grained region, strain localization is suppressed at the surface. Therefore, the coarse grained region becomes hardened, while the surface becomes softened during tensile testing of the gradient structure according to this theory. Early evidence of this theory was shown via softening of the surface in post mortem analysis, and some computational modeling has predicted a gradient in geometrically necessary dislocations [14,24]. Further evidence of this theory was observed by comparing microhardness and grain sizes across gradient structured copper before and after tensile testing [21]. After testing, this grain size

increase led to a reduction in microhardness from 1.6GPa to 1.2GPa and was accompanied by an enhanced texture along the tensile direction. Although grain growth of metastable nanocrystalline grain is usually a thermally driven process, strain induced grain growth has been observed, primarily in nanocrystalline aluminum [25–27]. However, no other studies in the gradient structure literature have observed similar results, though this does not preclude this mechanism from operating in addition to others reported here. Additionally, the experimental evidence used to support this claim comes from the necked region of the gradient structure, which is beyond the strain of uniform elongation. As a result, majority of the plastic behavior of gradient structures has not been studied relative to this mechanism. Because the magnitude of this effect has not been quantified, its effect on gradient structure plasticity cannot be deduced relative to other deformation mechanisms known to operate within the gradient.

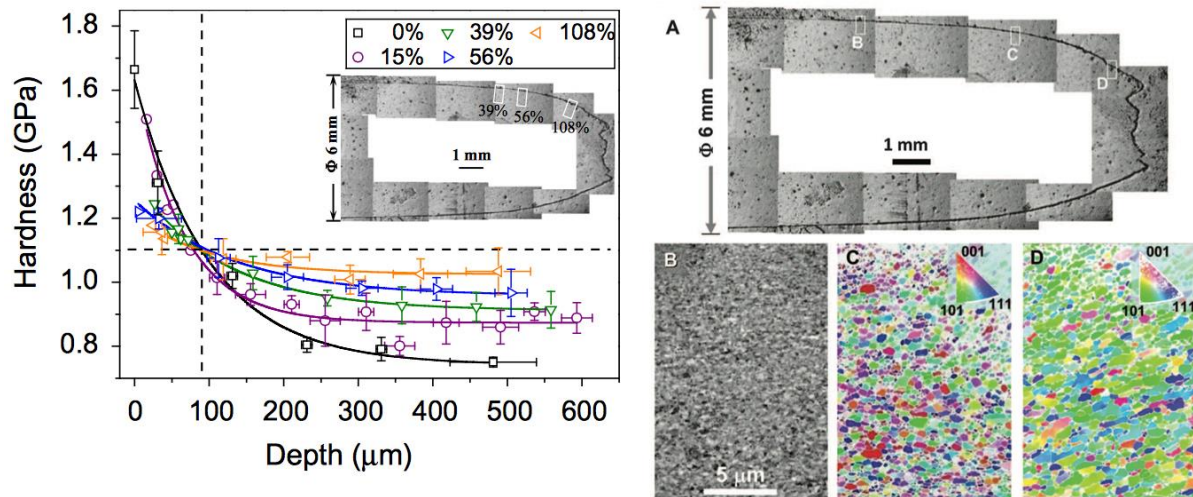


Figure 1.6 Strain induced grain growth and corresponding softening which accounts for extraordinary strengthening observed in gradient structured nanocrystalline copper [14,22].

#### 1.3.4 Residual Stress Effect

One often overlooked effect in the field of gradient structures is the effect of residual stresses on the tensile properties of the gradient structure. In the field of ceramics, residual stresses are often used to improve the toughness of glass, and a similar effect has been seen in a pseudo-gradient structured metallic glasses [28,29]. In the latter case, shot peening of the tensile sample led to a tensile surface stress, causing an improvement in uniform elongation from 10% to 23%, accompanied by improvements in yield and tensile strengths [28]. In conventional metals, gradient structured nickel exhibited compressive stresses three times higher than the yield strength at depths 150 mm from the surface [30–32]. The compressive stress field extended to depths >500mm and led to yield strength improvements of ~2x. Finite Element Modeling indicated that 40% of the strengthening was caused by the residual

stresses, while the remaining 60% came from work hardening. It is well known that the SMAT process inherently creates high compressive residual stresses at the surface and that this stress gradient is very similar to that created by conventional shot peening [33–37]. Considering the correlation between yield strength and compressive residual stresses found in shot peening, some strengthening effect should be expected in gradient structures [35].

If the compressive stresses are sufficiently high at the surface of the gradient structure, then it must be balanced by a residual tension stress within the interior matrix. As a result, when deformed in uniaxial tension, the tensile stresses quickly exceed the yield strength of the material, causing the interior to begin plastic deformation, while the surface is still deforming elastically. This low strain non-uniform deformation has been predicted to reduce the elastic modulus, and causes a strain gradient to develop prior to yielding [30]. Once both regions are deforming plastically, the residual stress has a negligible effect on plasticity relative to other mechanisms [38,39].

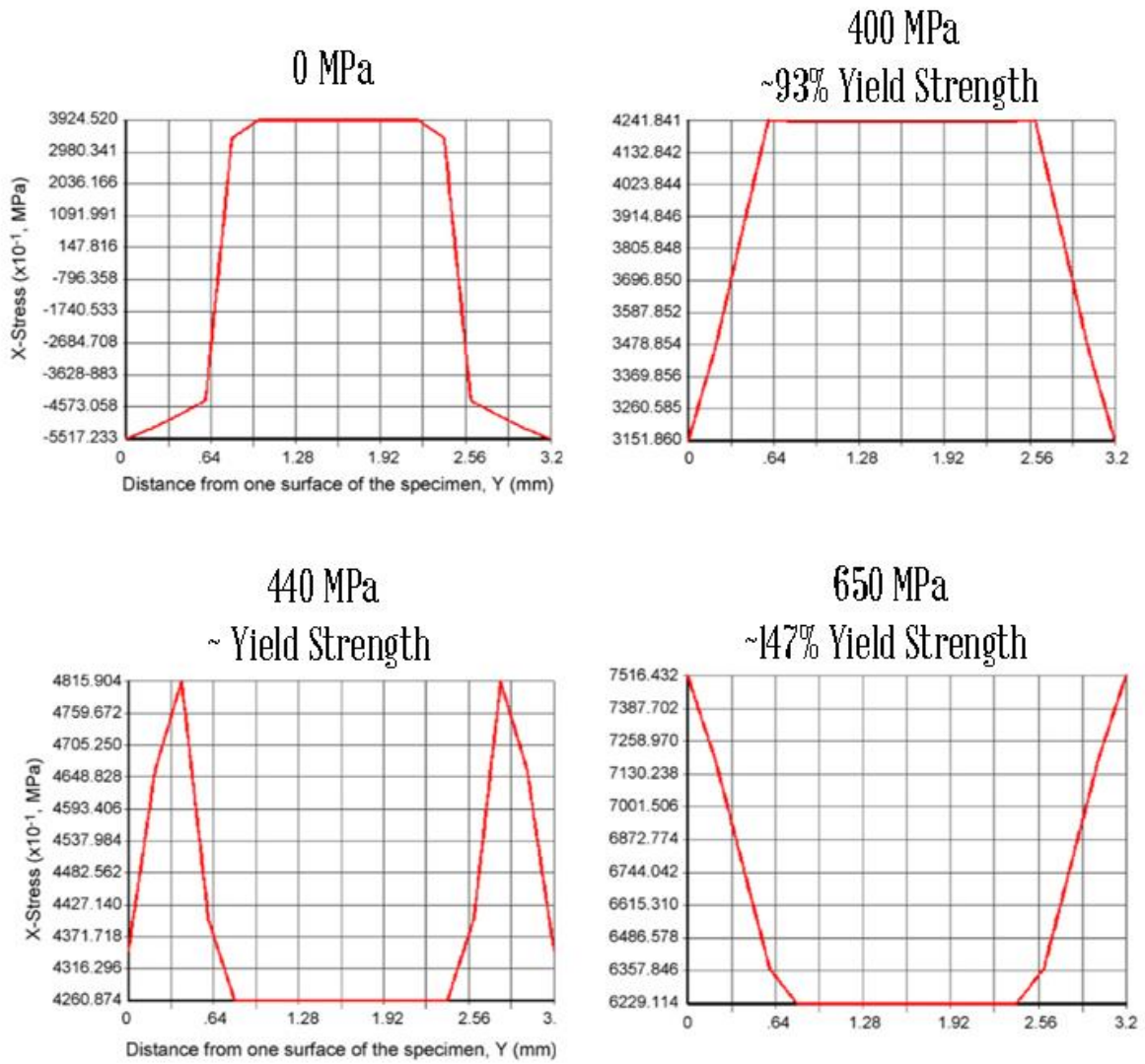


Figure 1.7 Finite Element Modeling of the evolution of residual stresses induced by SMAT at various tensile loads before and after the onset of plastic deformation [30].

## 1.4 Plasticity and Texture

Crystallographic “texture” is generally defined as the preferred orientation or orientations in a material [40]. As most materials are comprised of individual crystallites or grains, the orientation of these grains can have profound implications for material properties, particularly if the degree of texture is pronounced. This is important because texture can give rise to anisotropic properties from materials with isotropic crystallites. One of the most common examples of texture induced anisotropy is in drawing of aluminum cups. Face centered cubic (FCC) Aluminum is highly symmetric and generally does not produce great anisotropic properties along any crystallographic direction [41,42]. However, after rolling, the material becomes highly textured with preferred orientations aligning with the rolling direction and transverse direction. After cup drawing, the plastic flow of material produces “ears” in the aluminum cup corresponding to the previous deformation routes [43]. Similarly, one dimensional loading like wire drawing produces a single axis of symmetry and a “wire texture” [41]. Although complicated, texture evolution by means of plastic deformation is worth introducing in some detail as it will be important in later chapters.

### *1.4.1 Slip in Single Crystals*

Single slip in metals occurs on the close packed plane and close packed direction within a single crystal. When a sufficient load is applied, the projection of the applied stress onto a given slip system is needed to determine which system will operate:

$$m^s : \sigma^c = \tau^s$$

Where the inner product  $m^s : \sigma^c$  is the projection of the applied stress onto a given slip system, giving the necessary critical resolved shear stress to operate slip,  $\tau^s$ . This dependence of slip on the shear stress gives rise to the Schmid Law

$$m = \cos\phi\cos\lambda$$

Where  $m$  is the so-called Schmid Factor,  $\phi$  is the angle between the slip direction and applied stress and  $\lambda$  is the angle between the applied stress and glide plane normal. From this model, the Schmid factor has a maximum value of 0.5 corresponding to the slip plane normal and slip direction both lying 45 degrees from the applied stress. It is clear from this construction that the operating slip system is strongly dependent on both the direction and magnitude of stress that loads a crystal.

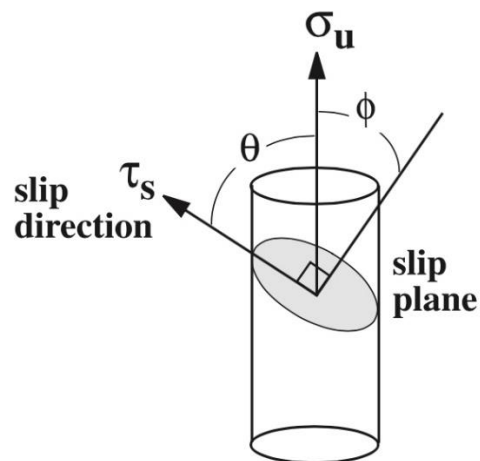


Figure 1.8 Cartoon showing the relationship between an applied stress,  $\sigma_u$ , and its angles relative to the slip plane and direction.

### 1.4.2 Slip in Polycrystalline Metals

In polycrystalline metals, the kinematics of slip are far more complicated due to the interaction between grains, and the lower shear stresses induced on preferred orientations relative to the direction of applied stress. This causes some grains to undergo multiple slip before others due to the lower critical resolved shear stress. At the same time, plastic deformation requires that grains deform coherently. Under these constraints the Taylor factor was derived, which only considers the component of the slip system that does work.

$$M = \frac{\sigma_c}{\tau_c}$$

Where  $M$  is the so-called Taylor factor,  $\sigma_c$  is the relative strength of the crystal and  $\tau_c$  is the shear stress on a given slip system [44]. Essentially, the Taylor factor predicts the readiness for slip within a single grain, where higher Taylor factors imply a high strength in a given loading direction for a given slip system. Using the Taylor model, texture evolution, and the effect of texture on mechanical properties has been mapped for a wide variety of metals [43,45–47]. Because rarely does slip occur only on one slip system in one direction, the crystallographic transformation a crystallite undergoes will be accompanied by a lattice rotation. Understanding multiple slip and its effect on reorienting the crystallography of a grain will be important for this work.

### 1.4.3 Dislocation Type

In 1952, Nye published his seminal work on statistically stored dislocations (SSDs) and geometrically necessary dislocations (GNDs)[48]. Although both SSDs and GNDs contribute to the total dislocation density, the GNDs are defined as the dislocations remaining when constructing burgers circuits with the deformed metal. The so-called Nye Tensor,  $\alpha_{ij}$  is the dislocation density tensor and is constructed using these burgers circuits within a dislocated crystal.

$$\alpha_{ij} = \sum_t b_i^t l_j^t \delta(x - x_t)$$

Where dislocations are described by their burgers vector,  $b_t$ , their line vector,  $l_t$  is the burgers vector at position  $x_t$ . This derivation was extended for GNDS where the Nye tensor can be reduced in the absence of elastic strain, to

$$\alpha_{ik} = k_{ki} - \delta_{ki} k_{mm}$$

Where  $K_{ki}$  is the curvature tensor of the lattice [49,50] . From a crystallographic perspective, this curvature tensor indicates that GNDs manifest themselves as a lattice rotation within a grain. On the other hand, the SSDs represent a pair of dislocations with opposite burgers vectors, which causes their net strain to accumulate to zero. GNDs are important because they accumulate in part to maintain coherency between grains during plastic deformation [50]. Because GNDs develop in the presence of strain gradients, they can be used to characterize non-uniform plastic deformation [50,51]. In fact, gradient structures are known to exhibit high volumes of GNDs at the deformed surface, before and after tensile testing, which may provide clues to the deformation mechanism [16,24,52–54]. Interestingly, there

has been tremendous headway made in the field of high resolution EBSD in reconstructing not only the GND density, but the entire Nye tensor across mapped regions [55–58]. These developments and their application will be discussed in future chapters.

#### *1.4.4 Texture Interpretation*

Interpreting texture is often done using pole figures, inverse pole figures, or using the orientation distribution function (ODF). All of these presentation methods are designed to relate the crystallographic indices, or Euler angles ( $\psi$ ,  $\phi$ ,  $\theta$ ) of the crystallites to physical indices ( $x$ ,  $y$ ,  $z$ ), making their direct interpretation challenging. In general, the pole figure and inverse pole figures are simplest to visualize. Pole figures project a single crystallographic orientation onto a sphere of “real space” coordinates  $x$ ,  $y$ , and  $z$ . This construction is made for different crystallographic directions, typically those with the highest symmetry. Alternatively, the inverse pole figure projects all crystallographic orientations onto a single slice of the stereographic projection along the real space axes  $x$ ,  $y$ , and  $z$ .

**Another reason texture is of interest to current lines of research is due to the extraordinary lack of information available about texture evolution in the nanocrystalline regime [59].** Often, nanocrystalline regions are presented as “randomly oriented” which is statistically highly improbable in the field of texture analysis. The few studies investigating texture as it relates specifically to SPD suggest conflicting findings. In HPT, both a diffuse, random texture and a very strong wire texture are reported for pure Ni [60]. ECAE on the other hand, appears to generate strong textures in the UFG regime that

weaken as the grain size approaches 100 nm [61]. In SMAT, it appears that the texture can be both strengthened and weakened depending on the material and grain size of the region of interest [62,63]. Considering the variety of deformation mechanisms operating at the nano-scale and the enormous implications texture anisotropy has on mechanical performance, investigations in this field are of immediate importance to the scientific community.

### 1.5 Motivation

As is often the case in science, exciting laboratory results are often published without undergoing systematic investigation of the mechanism leading to the unexpected behavior. It is much easier to find a scientific curiosity than it is to definitively pin down the underlying principals at hand. In the SMAT literature, this convoluting effect has been compounded by proprietary equipment that prevents new researchers from evaluating the findings, making experiments all but impossible to reproduce. For example, in an overview of the SMAT process, the accelerating frequency ranges from 50 Hz to 20,000 Hz with ball sizes ranging from 1mm to 10 mm [10]. Instead of listing arbitrary experimental conditions, it is the opinion of the author that more fundamental material properties should be used to study the SMAT process. **As a result, the first objective is to systematically investigate the SMAT process and its effect on metallic systems.**

Because the deformation mechanisms of nanocrystalline metals are poorly understood, the interaction of these nanocrystalline regimes with their coarse grained counterparts is a field of study that is in its infancy. The interaction between the various

regions within a gradient structure presents a complex multi-scale problem where no current model of mechanical behavior is sufficient. However, an understanding of the governing mechanisms may be developed by investigating the dislocation accumulation and crystallographic relationships that evolve within the gradient. **Therefore, the second objective of this work is to investigate the microstructural evolution of gradient structures under load.**

## **2 Synthesis and Characterization**

### **2.1 SPEX Milling of Flat Samples**

The first equipment that was used for generating SMAT microstructures was a system that employed an ultrasonic horn that resonated at 20kHz to accelerate 3mm balls within a confined chamber. It was quickly discovered that this system induced nanocrystalline layers in very small regions and was only effective for systems with low stacking fault energies like brass and austenitic stainless steels, or with certain second phases [13,64]. Despite numerous processing schemes, conventional metals like aluminum, steel, copper, and iron did not develop nanocrystalline surfaces. It was determined that the impact energy was not high enough, and that by using larger balls (which were not accelerated in the SMAT machine due to the high frequency) more impressive gradient structures could be produced. In fact, some of the earliest SMAT successes in literature were with larger balls and lower impact frequencies [65].

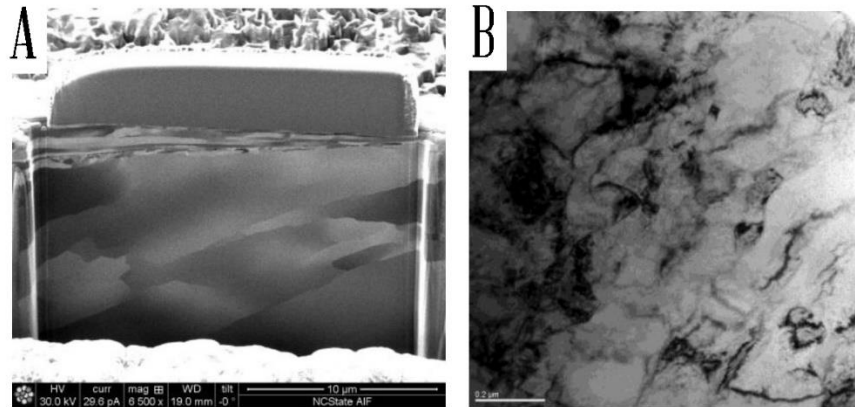


Figure 2.1 (a) Cross sectional FIB image of 99.9% Iron SMATed for 15 mins at 20kHz showing very little grain refinement at the surface. (b) TEM confirms that the grain size is not significantly reduced at this condition.

Due to these reasons and others, it was determined that a SPEX mill, typically used for milling powders, may be suitable for replicating SMAT research without building new equipment. The 8000M Mixer/Mill SPEX machine holds an enclosed vial that shakes in multiple directions at 1060 cycles per minute. By replacing the hardened steel lid with a plate of metal, the enclosed balls rapidlypeen the surface with a large number of impacts, which is directly related to the number of balls. This technique has been used by other researchers to study nickel, aluminum, and iron in a similar fashion [66–68]. As will be shown in following chapters, this procedure greatly improved the depth of the gradient, the degree of grain refinement, and the hardness of the surface layer tremendously.



Figure 2.2 (a) the SPEX vial typically used for high energy ball milling of powders. (b) Replacing the lid with a plate of a material naturally creates SMAT microstructures.

### 2.1.1 *Effect of Ball Size*

Although some systematic studies have been used to optimize the SMAT conditions, there is little information on practical considerations for generating nanostructured gradient structures in the lab. Therefore, it was important to develop a high level general knowledge of the effect of various conditions on the SMAT microstructure. Aside from variations in ball composition (only stainless or hardened steels were used in these studies), the size of the ball is directly proportional to the energy imparted during impact. Because the frequency of oscillation is fixed in a SPEX mill, the ball size is the only variable affecting the imparted

energy. First, a plate of a general low carbon steel was SMATed for 60 minutes using balls 1/8" in diameter and then another identical plate was SMATed for 60 minutes using balls 1/2" in diameter. Cross sectional samples were imaged using Scanning Electron Microscopy (SEM) to determine the depth of the deformed region.

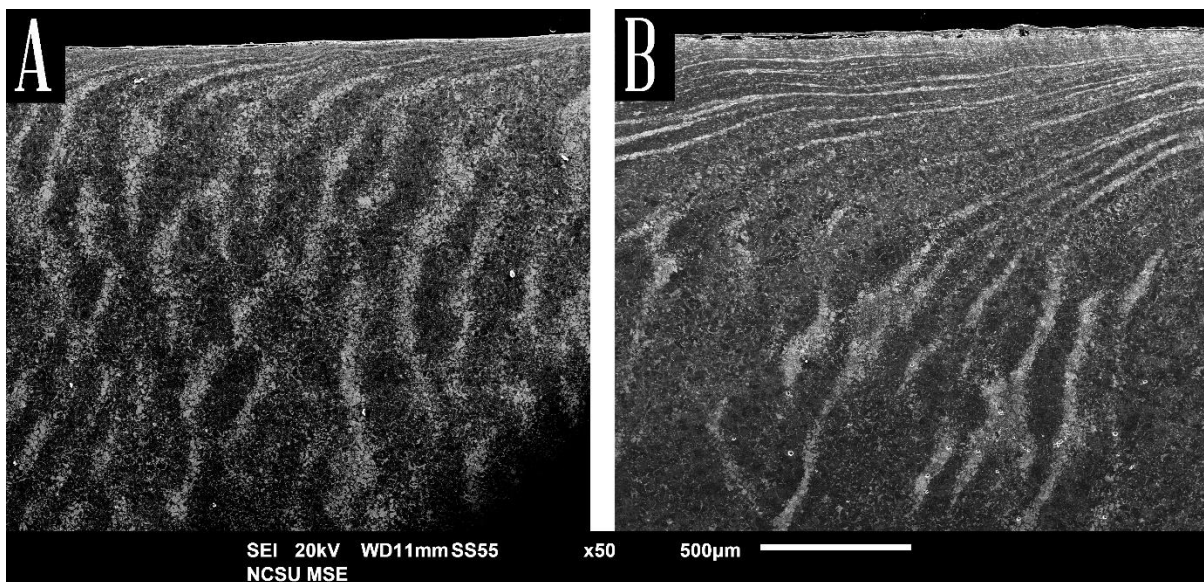


Figure 2.3 (a) Low carbon steel SMATed for 60 minutes using (a) 1/8" stainless steel balls and (b) 1/2" stainless steel balls.

As can be seen, the larger ball size shows a deeper deformed layer at the surface of the sample, as evidenced by the bending of the cementite (white colored) grains. Roughly speaking, the deformed region was calculated at 100 micrometers deep for 1/8" balls and 500 micrometers deep for 1/2" balls. The surface was also considerably rougher for larger balls. However, it was difficult to discern grain size using SEM due to the poor quality of etched

surfaces. Therefore, the top surface was analyzed using Focused Ion Beam (FIB) where grain contrast arises due to the crystallographic orientation with the ion beam.

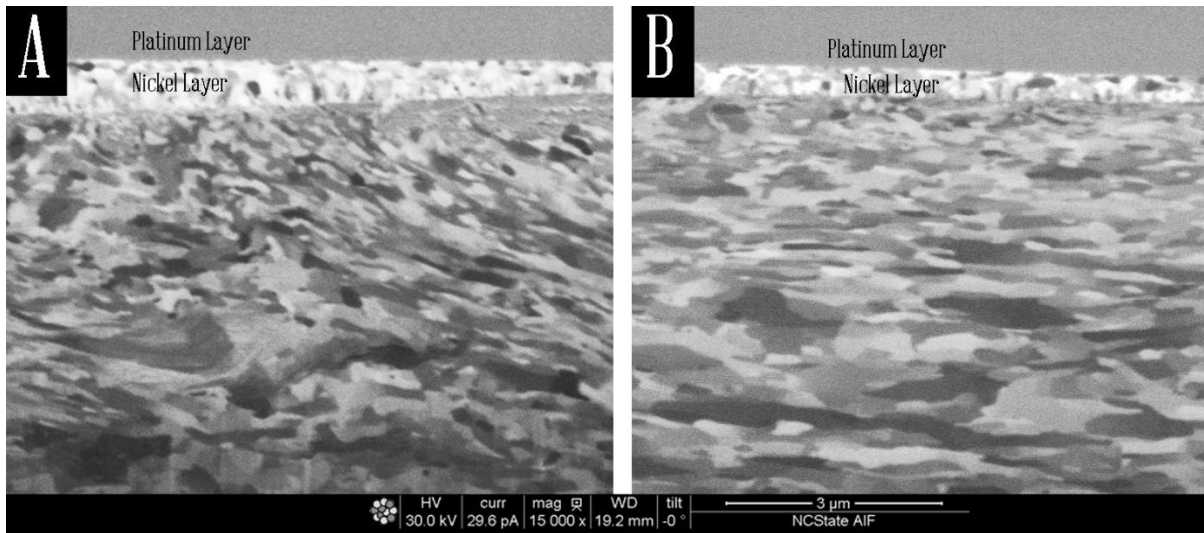


Figure 2.4 Higher magnification ion channeling contrast of the very top SMAT surface processed for 60 minutes with (a) 1/8” stainless steel balls and (b) 1/2” stainless steel balls.

Interestingly, the ball size did not appear to have a great effect on the degree of nanocrystallization at the surface of the SMAT sample. In both cases, the grain size is in the UFG regime with local regions exhibiting smaller grain sizes.

### 2.1.2 Processing Time

Clearly, the degree of deformation must be enhanced with increasing processing time, although the depth of the deformed layer does not appear to be significantly altered. This is evidenced by the bending of cementite grains approaching the surface of the sample. At higher magnification, it is apparent that the length of processing time decreased the grain size at the surface as well. Discussions of this effect will be expanded in following chapters.

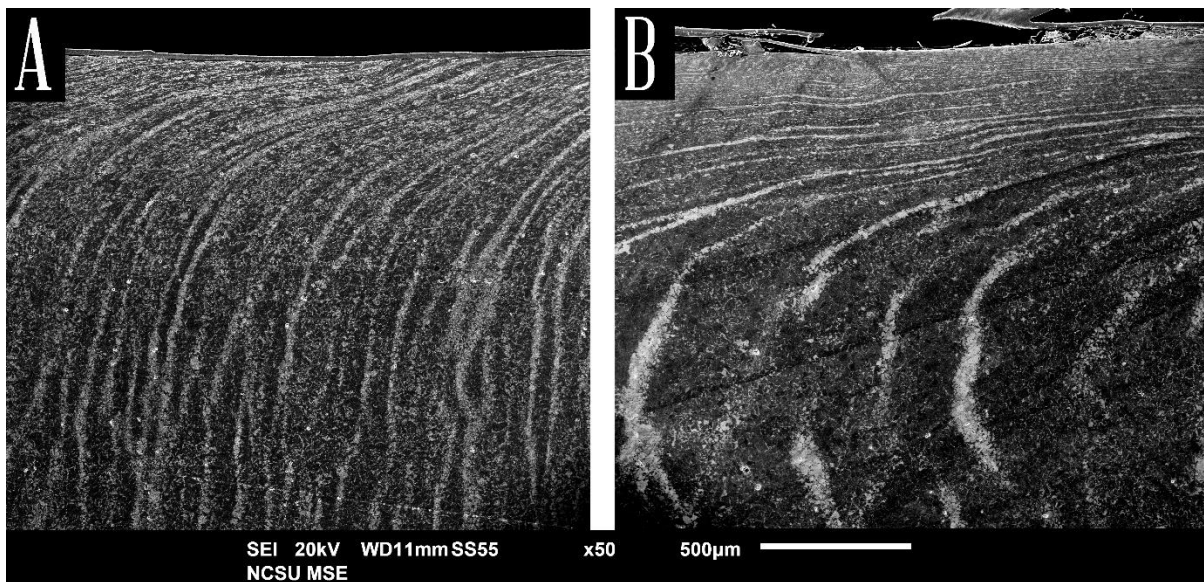


Figure 2.5 Low carbon steel SMATed with 1/2” stainless steel balls for (a) 30 minutes (b) 120 minutes.

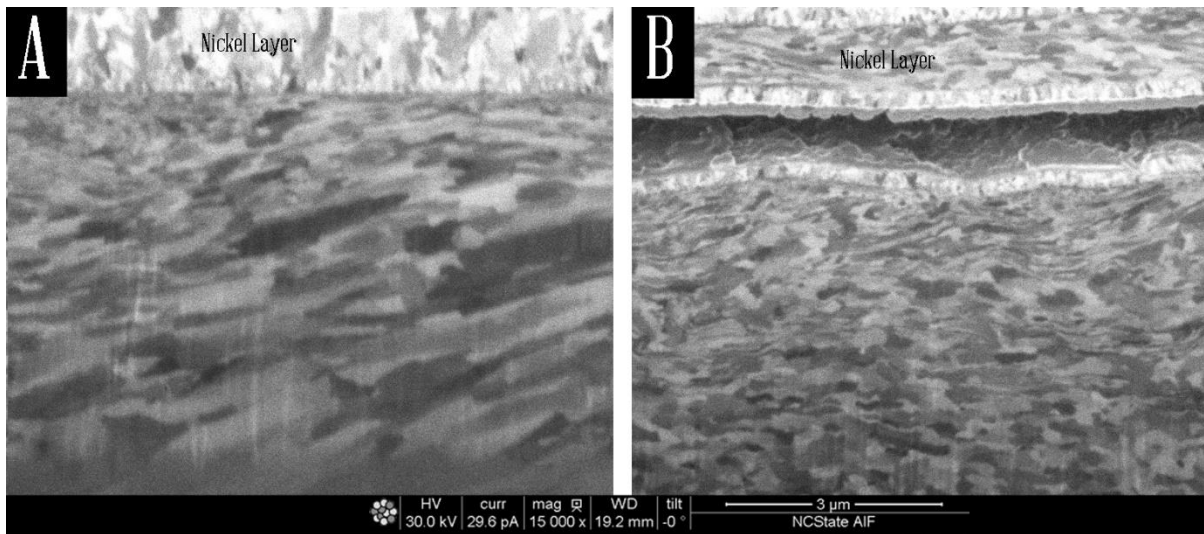


Figure 2.6 Higher magnification ion channeling contrast of the very top SMAT surface of a low carbon steel processed with 1/2” stainless steel balls for (a) 30 minutes and (b) 120 minutes.

## 2.2 SPEX Milling of Round Samples

The SPEX vial provides a simple and effective tool for creating gradient structures, but round samples require continuous rotation to avoid non-uniform deformation. Therefore, a new vial had to be created capable of generating SMAT microstructures on round samples. Although various permutations and equipment configuration were attempted, a custom vial resembling a standard SPEX vial with a hole drilled through the side was sufficient for this research. Because the SPEX process creates complex vial movements and ball dynamics, the oversized hole through the vial allowed the round samples to naturally rotate during processing. For most of this work, ten 1/4” stainless steel balls were used in the processing, and it was observed that round samples were uniformly peened (100% coverage) after 45

seconds using these conditions. Future modifications to the vial will need to include bearings for fixing the sample within the vial as the tolerance needed for sample rotation also causes some of the energy of the ball impacts to be lost.



Figure 2.7 (a) A custom SPEX vial used to process round samples. (b) An aluminum rod after SMAT processing in the vial for 5 minutes.

### 2.3 Introduction to EBSD

EBSD is a unique tool that couples high spatial resolution, with rich crystallographic detail in a single data set [69]. Prior to its commercialization, TEM or high resolution SEM were the usual tools needed for microstructural analysis at the nano scale, but these tools lacked crystallographic information. On the other hand, X-ray diffraction provided very precise data on the texture, lattice parameter, and orientation relationships, but produced data from a large volume of material. In EBSD, the electron beam is rastered across the sample, causing the ejection of elastically and inelastically scattered electrons, which are collected by the various detectors in the microscope. When the sample is tilted to  $\sim 70$  degrees, the incident electron beam ejects elastically scattered electrons at Bragg conditions, forming a pair of Kossel cones that corresponding to the miller indices of the diffracting planes. The intersection of the Kossel cones with the phosphor screen causes the Kikuchi lines to appear. After performing a Hough transform on the collected pattern, the Kikuchi lines are indexed. The relationship between the unit cell coordinates  $(h,k,l)$  and real space coordinates  $(x,y,z)$  are given by the Euler angles  $(\phi_1, \Phi, \phi_2)$ . By calculating the Euler angles across a scanned region, EBSD is able to acquire both high spatial resolution, and rich crystallographic data simultaneously

There are countless types of analysis that are possible with an EBSD data set. The pole figures, inverse pole figures, and Orientation Distribution Function (ODF) can be easily constructed. It is also possible characterize high angle and low angle grain boundaries, in addition to Coincident Site Lattice (CSL), and twin boundaries. Various texture components,

including the Schmid Factor and Taylor factor can be plotted for various grains, and qualitative strain analysis can be conducted by analyzing the pattern quality, which degrades for highly strained regions.

#### **2.4 Strain Analysis using High Resolution EBSD**

The Kikuchi patterns used in EBSD are affected by both plastic and elastic strain, so there have been numerous attempts to utilize this data to quantify strain in metals. Both elastic and plastic strain will affect the pattern quality, and this phenomenon has been used to qualitatively map strains by simply quantifying the contrast or blur of the pattern [70]. Elastic strain causes the unit cell to be distorted, which in turn can change the spacing and position of the Kikuchi bands on the phosphor screen. The lattice parameter shift is usually measured by XRD, but some strain sensitivity on the order of  $2 \times 10^{-4}$  have been reported, allowing small changes to be measured [70–73].

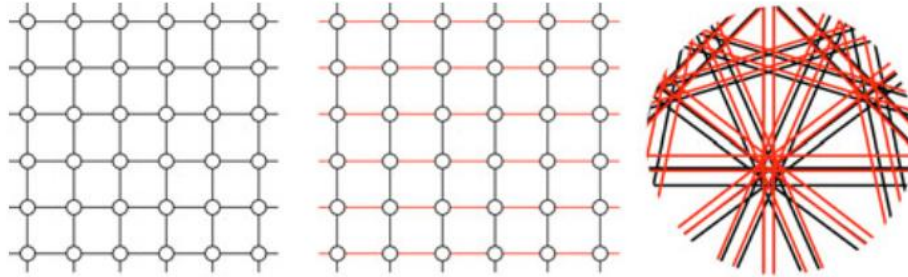


Figure 2.8 Kikuchi patterns can be rotated or skewed in the presence of elastic strain, schematically shown here with a perfect lattice (black) overlaid onto a distorted lattice (red)

[56].

In misorientation mapping, the relative shifts of the Euler angles within a grain are used to characterize the plastic strain. By using cross correlation to quantify the subtle deviations in Euler angles between adjacent pixels, six components of the curvature tensor can be quantified, leading to five components of the dislocation density tensor,  $\alpha_{12}$ ,  $\alpha_{13}$ ,  $\alpha_{21}$ ,  $\alpha_{23}$ , and  $\alpha_{33}$  [74]. The magnitude of the strain is very sensitive to acquisition parameters, but this relationship has been successfully used to plot local misorientations in a variety of metals [52,56,75]. For more accurate strain mapping, the cross correlation methods require a reference pattern to compare with collected patterns. As a result, there are two mindsets for how to collect a good reference. The simpler method is pick a reference pattern within a given grain as the unstrained pattern. There is commercial software available for this type of analysis, and strain sensitivities of  $2 \times 10^{-4}$  have been reported with this technique [55,70,76]. However, the strain calculated is actually relative, as in the case of severely deformed metals,

the software will still pick a reference pattern as unstrained. Another method is to simulate a strain free reference pattern using kinematical scattering theory [57,58,71]. This type of analysis provides more accurate results, but requires extensive simulation of experimental variables like aberrations, and pattern centering errors.

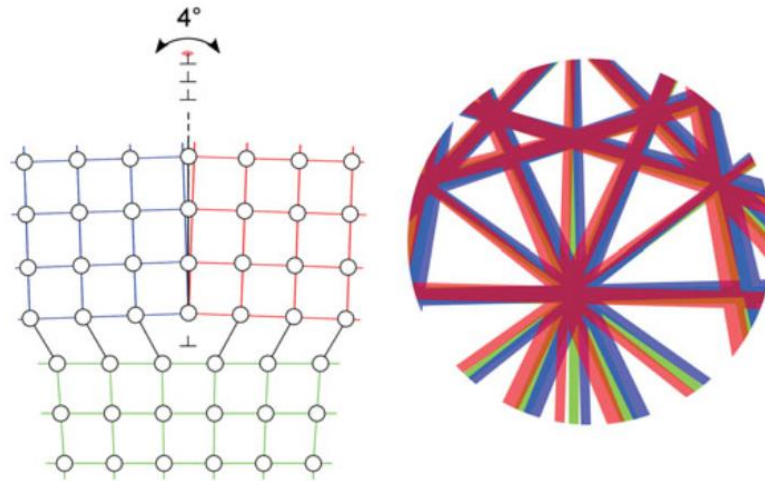


Figure 2.9 When an incident beam interacts with a dislocated crystal, the locally strained region around the dislocation core will produce slightly different Kikuchi patterns, shown here. This effect is very pronounced over regions with high dislocation density, like a grain boundary or slip band, causing poor pattern quality [56].

Strain analysis with EBSD provides a valuable tool in characterizing microstructural evolution in plastically deformed metals. Although still in its nascency, the technique has demonstrated successful mapping of the Nye and strain tensors along with GND density in a variety of materials including IF steel, aluminum, copper, and silicon [52,55,72,76]. Because non-uniform deformation is theorized to develop during tension of the gradient structure, and because residual stresses have been shown to profoundly affect tensile plasticity, strain analysis must be utilized to unravel the deformation mechanisms in gradient structured metals. In addition, because the gradient structure consists of a relatively strain free interior uniformly bound to a highly strained surface, the accuracy of the various strain mapping procedures can be assessed.

### **3 Flat Gradient Structures**

#### **3.1 Introduction**

The SMAT technique is ideal for systematic investigations of gradient structures due to the gradients in strain, strain rate, hardness, grain size, and hardening mechanisms throughout the deformed layer. In order to refine grain sizes to the nanometer scale, large strains and strain rates need to be applied [12,77,78]. It is well known that the shear component of the applied strain is directly correlated with dislocation slip and microstructure evolution. However, quantitatively mapping a single component of the strain tensor is challenging [79–81]. Markers and photographic evidence have been reported to extract the effect of shear strain on microstructure evolution, but they are not suitable for measuring shear strain in SMAT, due to the complexity of the process [82].

In this work, cementite bands are used as internal markers to quantify the shear strain at various depths of the surface, which is the first time shear strain has been quantitatively mapped in SMAT-processed samples. Additionally, the texture evolution is systematically characterized, which has rarely been studied in SMAT-processed structures but profoundly affects mechanical behavior [40,62,63,83]. The observations from this work elucidate the effect of shear strain on the development of texture gradient, microstructure gradient, and microhardness gradient in the SMAT-processed samples.

### 3.2 Experimental Procedure

Normalized steel plates with a composition of 0.14% C, 0.33% Si, 1.44% Mn, 0.08% Cr, 0.03% Ni, and balance Fe was used for this study. Samples were cut along the rolling direction so that the SMAT treatment would take place normal to the rolling direction. The pearlite was agglomerated into bands normal to the SMAT surface. The SMAT process was carried out using a SPEX 8000M Mixer/Mill by replacing the lid of the vial with ¼" thick plates of the sample to be treated. Samples were polished to 1200 grit, sealed in ambient atmosphere, and processed with three ½" 440C steel balls for 30, 60, and 120 minutes. Profilometry revealed that the roughest surface was the sample processed for 120 minutes and was roughened to an Ra of 8.8 µm after treatment. After treatment, cross-sectional samples were Ni-plated to protect the surface microstructure from edge rounding when polishing, and were imaged using a JEOL 6010LA Scanning Electron Microscope (SEM) at 20kV. Microhardness measurements were undertaken by averaging five hardness measurements at each depth with a Mitutoyo Microhardness Testing Machine Model HM-11 with a Vickers diamond indenter at a load of 0.05N. Grain size measurements were performed using the line intercept method from micrographs collected from the dual Beam FEI Quanta 3D FEG, the JEOL 2010 F Transmission Electron Microscope. Samples were prepared for EBSD imaging by conventional polishing followed by ion milling in a Fischione Ion Mill (Model-1060) at 5kV and 5° tilt for 45 minutes. An Oxford EBSD detector installed in the dual Beam FEI Quanta 3D FEG was used for collecting images.

### 3.3 Strain Analysis

Experimentally measuring a single component of the strain tensor is not a trivial matter. Attempts to discern the shear component of the tensor in severe plastic deformation processes have been undertaken primarily by simulation or calculation [12,79,81,84]. Experimentally, an imbedded pin method has been used to measure shear in accumulated roll bonding, where the interface of the pin can be used to map the shear strain, but this is not suitable for SMAT structures [82]. In normalized low carbon steels, clear bands of pearlite along the rolling direction ( $\alpha$ -iron +  $\text{Fe}_3\text{C}$ ) and ferrite ( $\alpha$ -iron) naturally act as markers in the microstructure and since the plates were cut normal to the rolling direction, these bands were perpendicular to the SMAT surface.

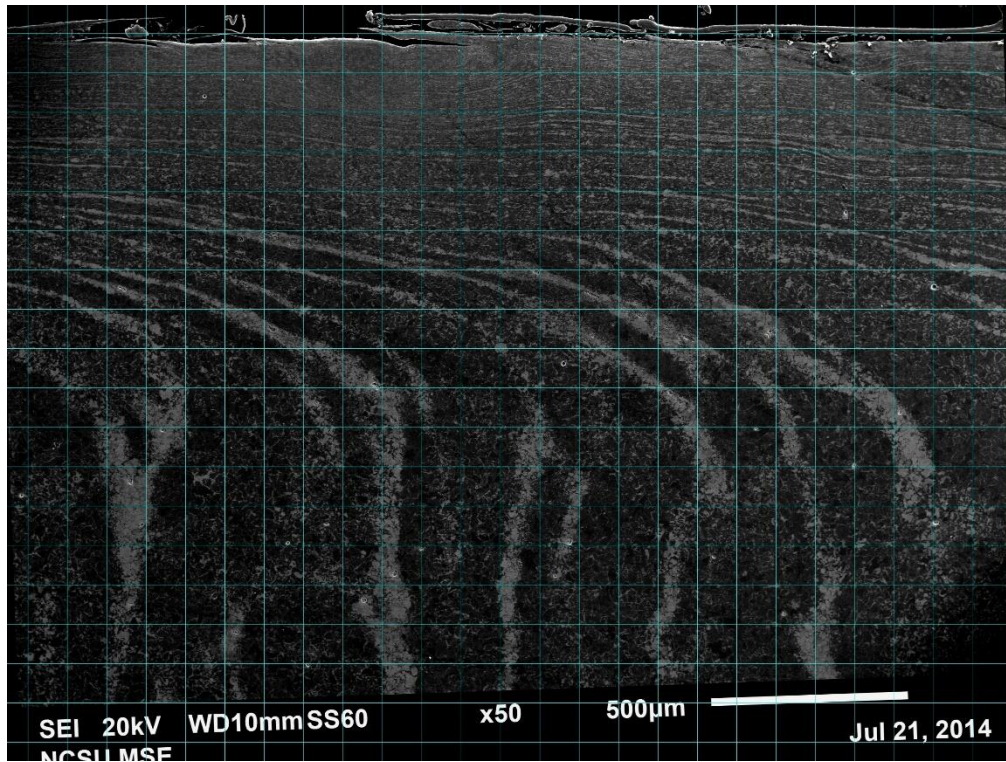


Figure 3.1 Grid overlay used to partition the SEM cross section of the SMAT microstructure for shear strain analysis. Note the surface is tilted in order to align with the grid and collect accurate measurements.

Because the shot impacts from SMAT repeatedly induce plastic flow in the surface, the top deformed layer is theorized to undergo high shear strains [13]. Therefore, simply mapping the slope of the deformed pearlite bands could yield the accumulated shear strain induced at various depths of the SMAT surface. First, a grid with 100  $\mu\text{m}$  blocks was overlaid onto the micrograph seen in Figure 3.1. Then, the average slope was measured in each of these regions to calculate the average shear strain at various depths. In this way, the shear strain plotted at 50  $\mu\text{m}$ , 150  $\mu\text{m}$ , 250  $\mu\text{m}$ , etc. represents the average shear strain at each 100  $\mu\text{m}$  interval. The result indicates that the shear strain increases exponentially near the surface, which is visually apparent in the cross-sectional SEM micrograph. A simple exponential fit ( $R^2 = 0.97$ ) was applied to the data in order to estimate the shear strain at discrete depths from the surface. Extrapolation of this data was used to estimate the shear strain at depths less than 100  $\mu\text{m}$  but it is not clear how big the error is from such an extrapolation. Surprisingly, in the 120 minute processed sample, the average measured shear strain at a depth of 50  $\mu\text{m}$  is 90, and the extrapolated shear strain in the top 10  $\mu\text{m}$  is 119, which is in the realm of shear strains measured in accumulated roll bonding and chip processing, as well as high pressure torsion [79,85]. Note that in the very top surface, e.g. at layer thickness close to the roughness, the current strain measurement may significantly underestimate the shear strain.

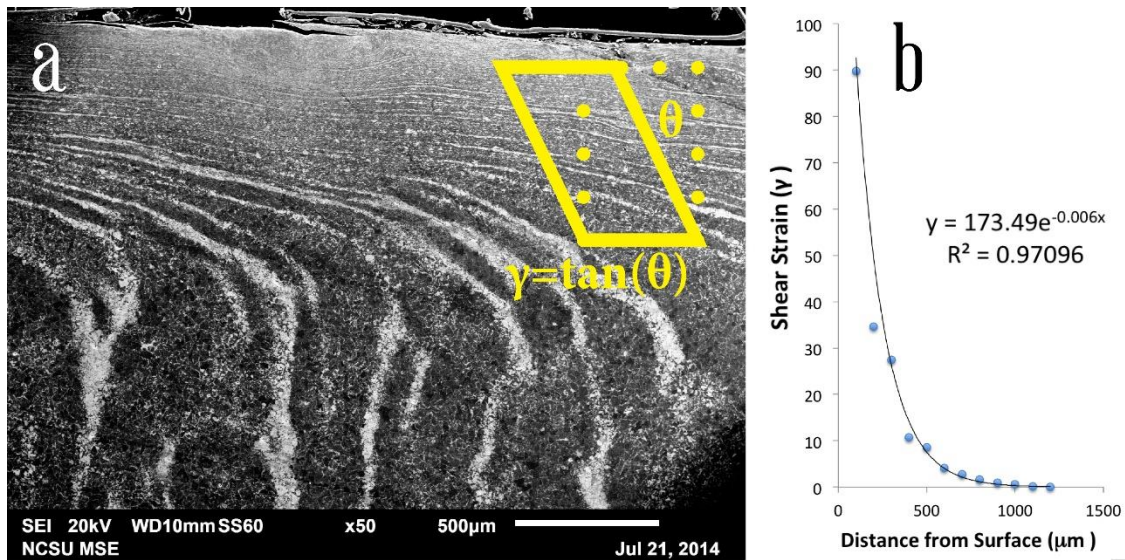


Figure 3.2 (a) An SEM image of the as-received SMAT surface. The inset shows how the slope of the cementite bands was measured in order to calculate shear strain  $\gamma$ . (b) The resulting data calculated at various depths showing a clear exponential increase in shear strain approaching the surface of the SMAT gradient [86].

One of the variables affecting microstructure development is processing time – specifically, the number of redundant impacts on a surface. In the shot peening literature, the term “coverage” is used to indicate what fraction of the virgin material was deformed by shots. Using 3 1/2” balls in the SPEX mill, this time was roughly 60 seconds. Therefore, samples processed for 30 minutes experienced roughly 30 redundant impacts at each location, and samples processed for 120 minutes experienced roughly 120 redundant impacts at each area. In cross section, the images showed clear microstructural evolution with more cementite bending with longer processing times.

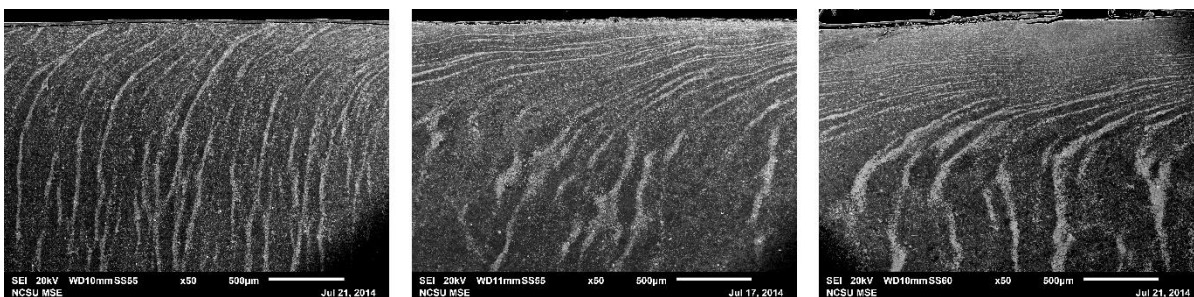


Figure 3.3 SEM cross sectional images of low carbon steel processed with  $\frac{1}{2}$ " balls for (left) 30, (middle) 60, and (right) 120 minutes.

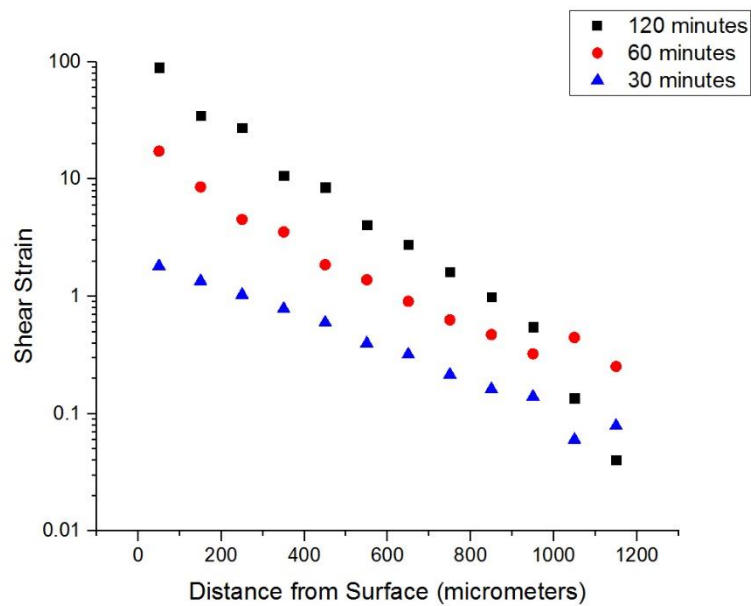


Figure 3.4 Shear strain estimates collected from the grid overlay method outlined previously.

Shear strain evolves exponentially approaching the surface, shown here plotted on a log scale.

### 3.4 Microstructural Analysis

Once the shear strain was calculated, grain size and microhardness measurements could be plotted to determine their relationship. Since the sample processed for 120 minutes showed the greatest shear strain, it was the only sample to be analyzed with grain size and microhardness analysis. Grain size was calculated using the line intercept method on EBSD, FIB, and HRTEM images at various depths within the sample. The figure below shows these relationships and a corresponding FIB micrograph of the gradient structure at the surface. Both hardness and grain size show a strong dependency on the shear strain, and the Hall-Petch plot shows slight deviation from the ideal linear trend.

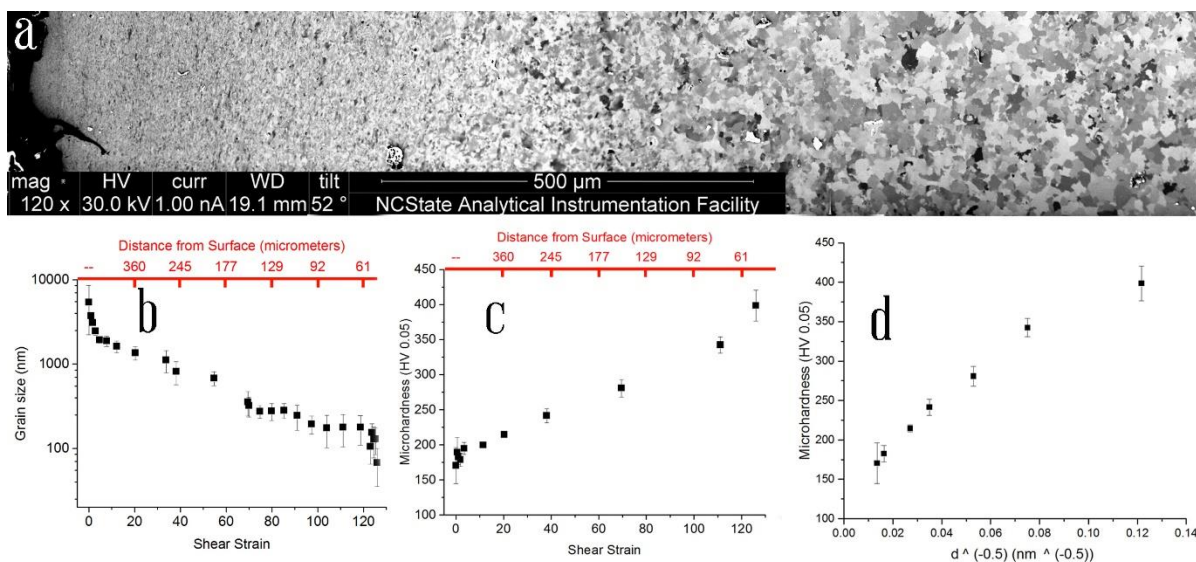


Figure 3.5 (a) A cross sectional FIB image of the SMAT gradient extending to depths greater than 500  $\mu\text{m}$ , (b) the strong linear dependence of microhardness on shear strain, (c) the dependence of grain size on shear strain, and (d) the microhardness approximately follows the Hall–Petch relationship [86].

This represents the first time that shear strain has been quantified in SMAT gradient structures. Although this analysis was not conducted for samples processed for times shorter than 120 minutes, it is expected that the hardening and grain size reduction relationship would be similar, since the effects of processing time have shown this relationship in other materials [10,77,78]. One interesting result is that at the top surface, with shear strains approaching 120, the average grain size appears to deviate from the linear trend. This region represents the nanocrystalline surface, which has often been reported to exhibit grain sizes  $<100$  nm for 5-50 micrometers [13,64,78]. In the nanocrystalline regime, mechanisms

governing the hardness and plasticity can differ from those in the coarse grained or ultrafine grained regions, so this well-defined nanocrystalline region is sometimes attributed to this phenomenon [10]. However, in steel, the presence of two phases can cause different nanocrystallization processes to occur given the interaction of the soft  $\alpha$ -iron and hard  $\text{Fe}_3\text{C}$  phase [13,65,81,87]. When the grain size of the  $\alpha$ -iron is reduced to the nanocrystalline regime, the hardness is dramatically improved, approaching that of the  $\text{Fe}_3\text{C}$  phase, which causes non-equilibrium microstructures to be developed including  $\alpha$ -iron with a supersaturation of carbon, or even FCC  $\alpha$ -iron [65,79]. Therefore, a microstructural gradient with respect to volume fraction of  $\alpha$ -iron and  $\text{Fe}_3\text{C}$  was expected to shed some light on this grain size gradient within the top 50 micrometers of the surface.

Using ion channeling contrast, the volume fraction  $\text{Fe}_3\text{C}$  phase was found to dwindle closer and closer to the surface as shown in the figure below. While this observation was only qualitative, FIB images at various depths show the evolution. It is well known that  $\text{Fe}_3\text{C}$  elongates, fragments, and subdivides into very small regions at high strains. Because the  $\text{Fe}_3\text{C}$  lamellae are on the order of 1000 nm in diameter to begin with, direct observation of their thickness was challenging even with high resolution FIB. In some cases at the top surface, the thickness of  $\text{Fe}_3\text{C}$  was only observable in TEM. Because the  $\text{Fe}_3\text{C}$  phase contributes to hardening considerably in low carbon steels, the thinning and reduction in size of this phase was not quantified for this study. Therefore, some of the variation in hardness and grain size could be accounted for by the lack of information gathered about this hard phase. Only the grain size effect of the  $\alpha$ -iron was considered in this analysis. Future studies

on the size and plasticity effect of  $\text{Fe}_3\text{C}$  within the SMAT layer should be conducted to better understand the mechanics of the SMAT layer in steels.

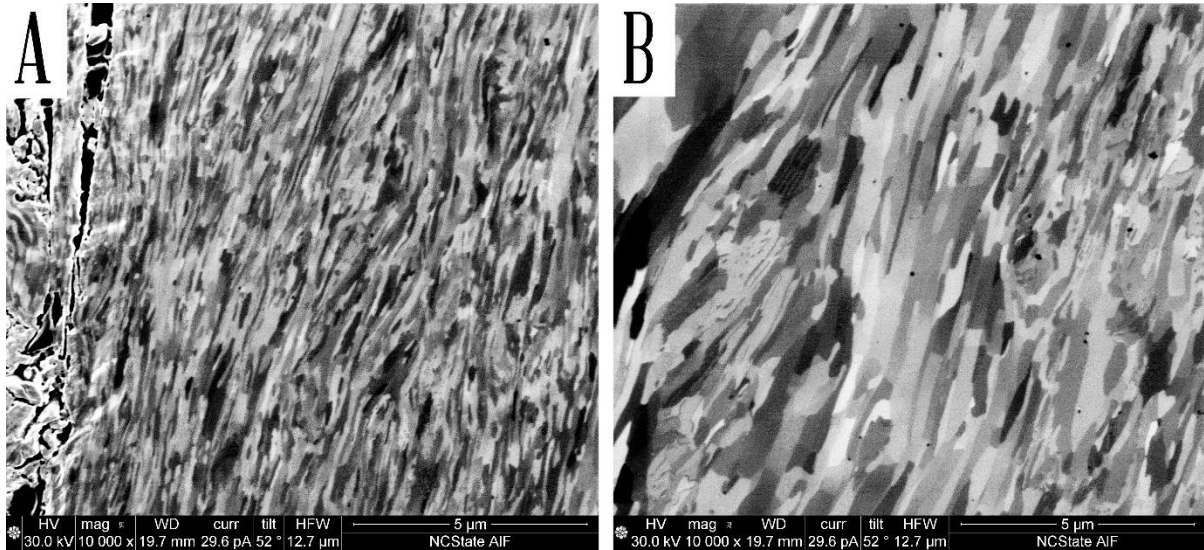


Figure 3.6(a) high magnification ion channeling contrast image of the surface, where no  $\text{Fe}_3\text{C}$  is observable. (b) An image of the same sample 100  $\mu\text{m}$  below the surface showing regions of elongated and fragmented  $\text{Fe}_3\text{C}$ .

Because the nanocrystalline grain size approaches the resolution limit of ion channeling imaging, TEM investigation of the top surface was undertaken to uncover the microstructural evolution at the very top surface of the SMAT layer. As expected, at the surface the grain size is dramatically reduced to 60 nm, as seen in the figure below. TEM samples confirmed that the grain size at the top surface was skewed, with some regions containing grains less than 10 nm, while other regions had grains 100 nm in diameter. This is

observation is clear in the dark field image, where nanocrystalline regions are intermixed with equiaxed grains 100nm in diameter, along with very thin, elongated grains of  $\text{Fe}_3\text{C}$ .

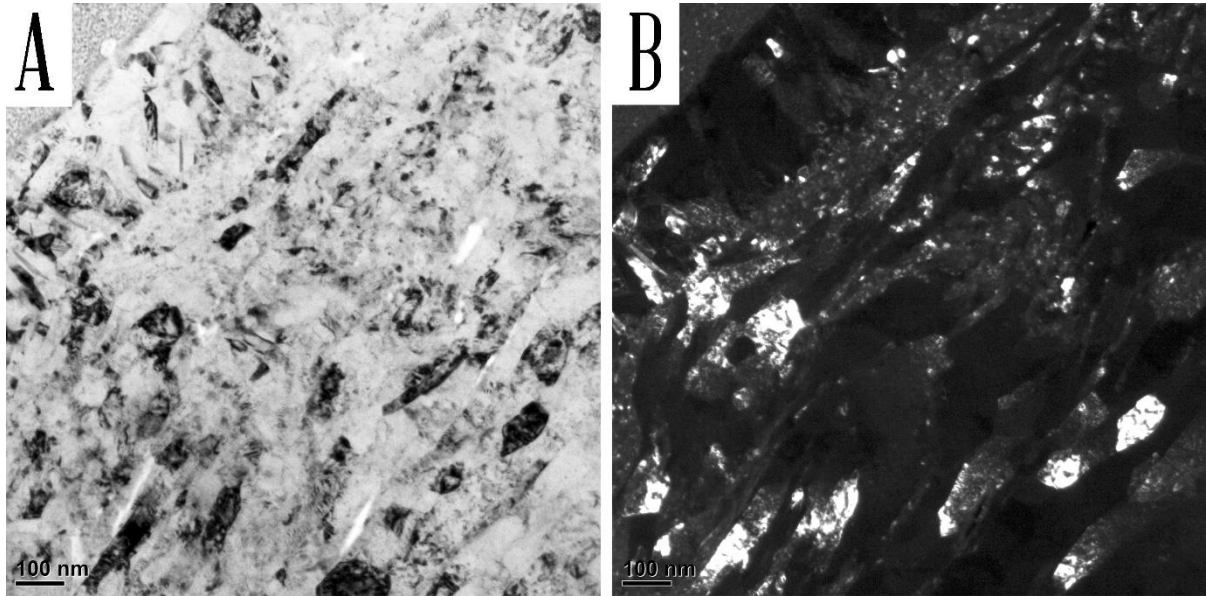


Figure 3.7 (a) Bright field and (b) corresponding dark field TEM image of the top surface.

Nanocrystalline grains <10nm in diameter are intermixed with 100 nm diameter  $\alpha$ -iron grains. It is also possible to discern several thin, elongated  $\text{Fe}_3\text{C}$  grains.

The distribution of grain sizes at the top 10  $\mu\text{m}$  of the SMATed surface was collected and plotted to get a sense of the data spread. Clearly, regions exhibiting grain sizes <10nm account for a relatively large volume fraction, though these are intermixed with larger grains of  $\alpha$ -iron. In carbon steels, the reduction of grain sizes to <10nm has been reported in regions subject to very high shear strains, and were first discovered in railroad tracks [79]. These

regions were called “white etching layers”, which consist of fragmented  $\text{Fe}_3\text{C}$  and even complete  $\text{Fe}_3\text{C}$  dissolution that leads to supersaturation of carbon in nanocrystalline  $\alpha$ -iron [80,87,88]. Interestingly, this type of microstructure is typically observed in high carbon steels, which would be consistent with theory of a supersaturation of carbon, since higher carbon steels would already have a higher volume fraction of  $\text{Fe}_3\text{C}$ , and therefore would have a higher chemical driving force for this reaction. Because this steel exhibits lower volume fractions of  $\text{Fe}_3\text{C}$ , it would be expected to have less regions exhibiting the nanocrystalline  $\alpha$ -iron with a supersaturation of carbon. TEM observation qualitatively confirms this observation, as the nanocrystalline regions were only found next to elongated regions of very thin (10-20nm) grains of  $\text{Fe}_3\text{C}$ , which is the necessary precursor to develop this phase [79,80].

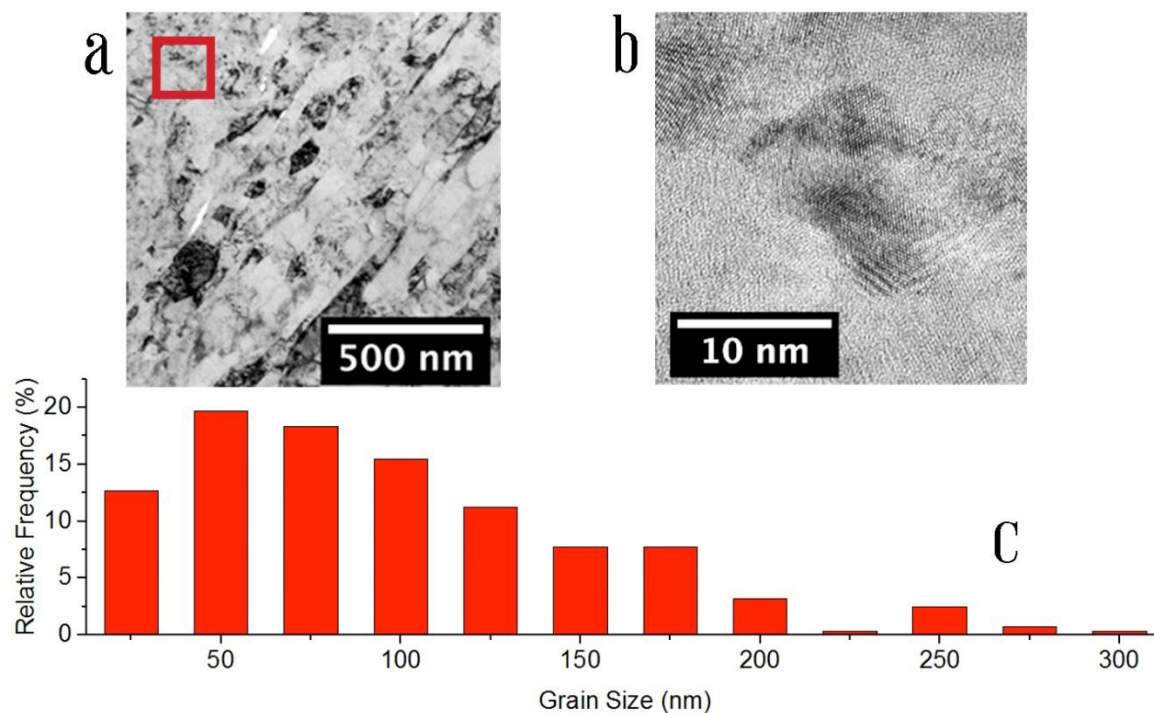


Figure 3.8(a) A representative image of the top surface shows regions with both nanocrystalline (<100 nm) grains and coarse grains intermixed. (b) High resolution TEM of the nanocrystalline region shows a single grain ~10 nm in diameter. This microstructure has been reported in steels subject to high shear strains and indicates partial decomposition of  $\text{Fe}_3\text{C}$ . (c) Grain size distribution at the top surface [86].

### **3.5 Texture Analysis**

Because SMAT is a complex deformation scheme consisting of compressive and shear strains at various strain rates, mapping the texture allows for a simple investigation on the underlying deformation schemes at various depths from the surface [10,40]. EBSD data also provides valuable information about strain accumulation, grain boundary character, grain size, and orientation relationships within the mapped region. At the top surface, a high resolution map showed a strong texture developed.

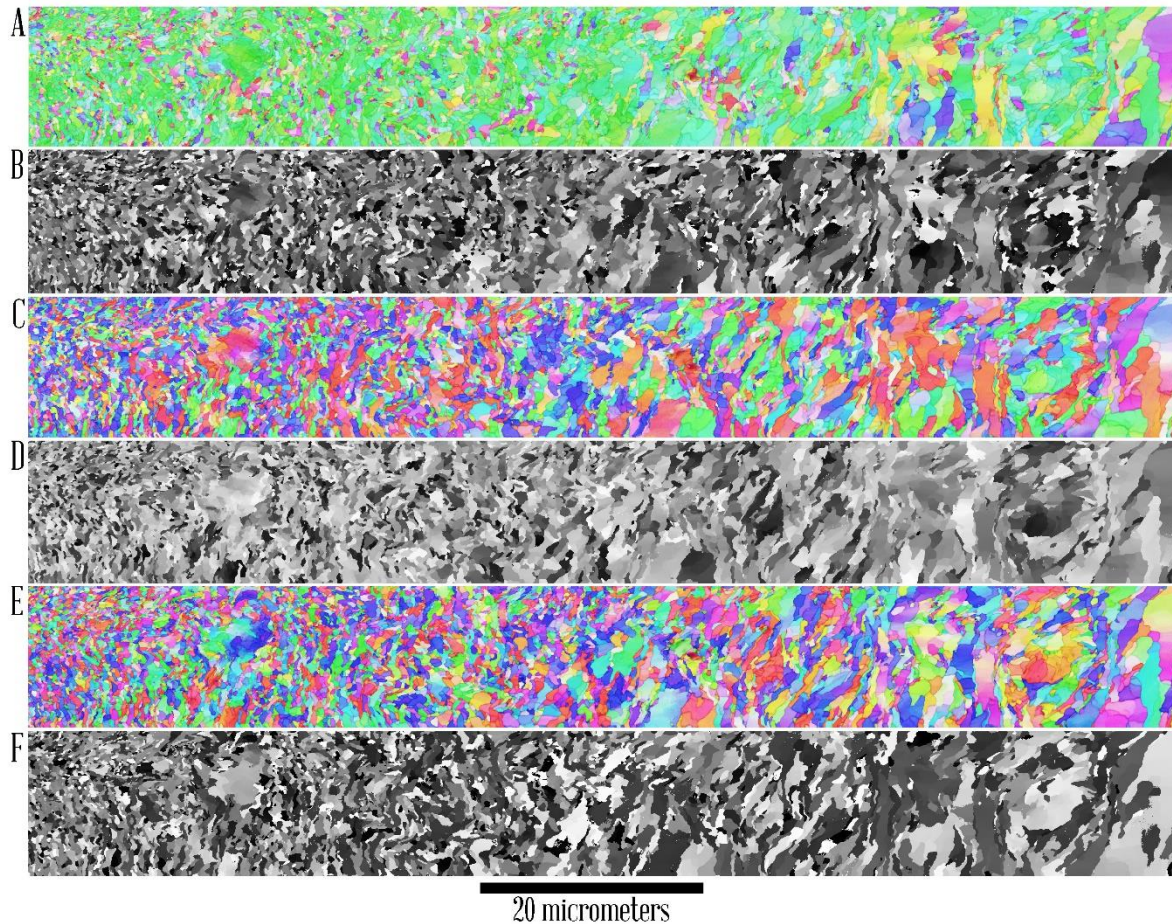


Figure 3.9 EBSD map of the top 60  $\mu\text{m}$  of the SMAT surface. Coloring schemes represent the orientation relative to the x, y, and z directions, for figures a, c, and e respectively, where the x direction is defined as the normal to the SMAT surface. (b, d, f) Coloring based on the value of each Euler angle within the SMAT surface.

Clearly, the projection along the X direction (normal to SMAT surface) exhibits a strong texture, as seen by the predominant,  $\{110\}$  orientation that is colored green in the image. The Euler angle projections are somewhat less informative, but are included to show

the capabilities of EBSD for mapping intrinsic crystallographic relationships within mapped regions. This map also shows regions at the top surface with grain sizes  $<100$  nm. This grain size is approaching the limits of EBSD for several reasons. The first is that the interaction volume from which orientation data is collected extends 10s of nm below the surface of the mapped region. This interaction volume is proportional to the energy of impacting electrons, which is controlled by the accelerating voltage. Second, because the sample tilt of EBSD is required to be 70 degrees, there is considerable enlargement of the spot size of the electron beam impinging on the sample. At higher beam currents, the minimum resolution is decreased, which, coupled with the high tilt angle, causes the back scattered electrons to be collected from a larger region. Therefore, EBSD resolution limits are usually linked to the spot size and number of pixels needed to index a single grain, which usually limits resolution to 20-50nm is the most extreme case.

The figure below shows an overview of the microstructural and textural development along the depth. The as-received material consists primarily of high-angle grain boundaries ( $>15^\circ$ ) and displays no strong texture. After SMAT, at 200  $\mu\text{m}$  below the surface, no strong texture can be determined, but the grain size has been reduced and clear subgrain boundaries ( $>2^\circ$ ) can be seen within large grains. At 100  $\mu\text{m}$  below the surface, there is a clear transition to a complex texture with  $\{110\}$  and some  $\{111\}$  planes // SMAT surface, and low-angle grain boundaries have evolved from the subgrain boundaries. At 50  $\mu\text{m}$  below the surface, although some residual  $\{111\}$  // SMAT surface texture can still be seen, the texture mostly transitioned to  $\{110\}$  // SMAT surface, which is a well-known texture for highly sheared  $\alpha$ -

iron [40,89]. At the top surface, the  $\{110\}$  // SMAT surface texture is further strengthened, and most grain boundaries have been converted to high angle. As can be seen in the figure below, the development of the texture of  $\{110\}$  // SMAT surface is preceded by diminishing  $\{111\}$  components from the depth of 100  $\mu\text{m}$  to the surface.

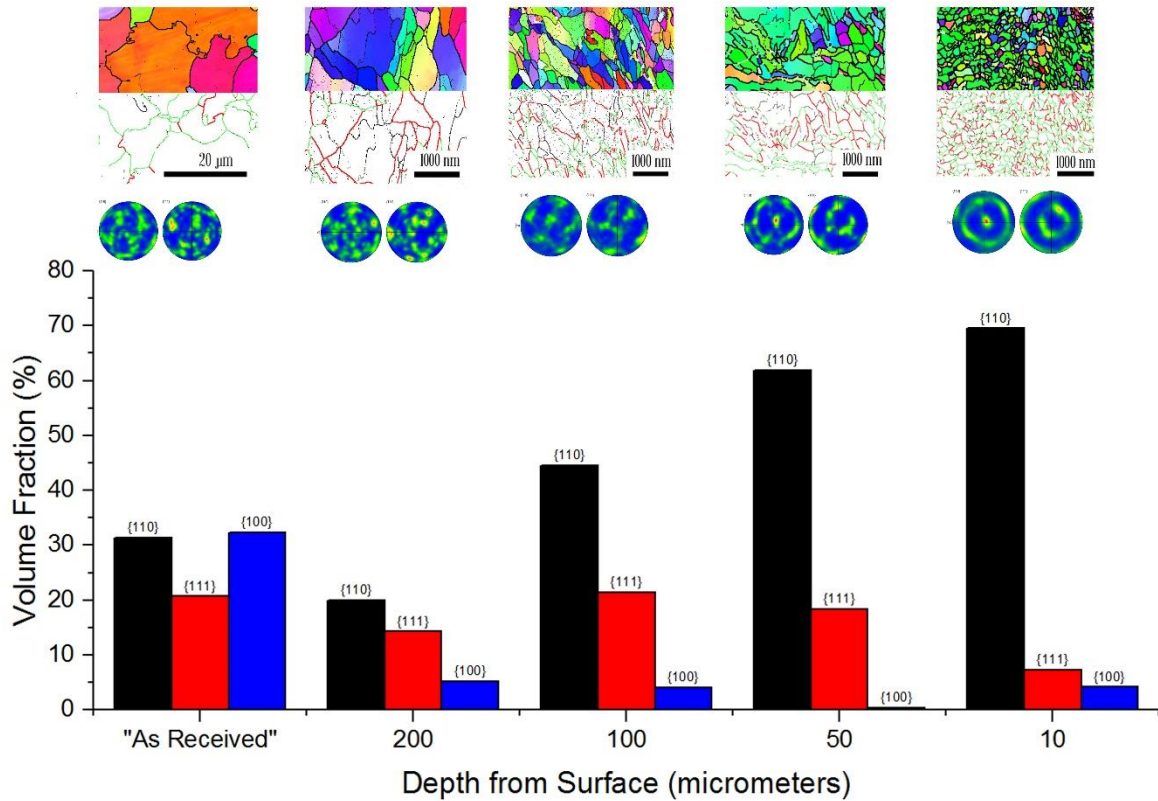


Figure 3.10 Development of microstructure and texture at varying depths from the surface. The percentage of grains indexed normal to the SMAT surface were calculated from EBSD maps and show the relative frequency of the  $\{111\}$ ,  $\{110\}$  and planes in  $\alpha$ -iron at various depths. Grain boundary maps indicate high angle ( $>15^\circ$ ) grain boundaries in green, low angle ( $2^\circ$ ) boundaries in black. Pole figures are projected normal to the SMAT surface, indicating a strong  $\{110\}$ // SMAT surface texture developed in the top  $50\ \mu\text{m}$  [86].

Texture develops when preferred crystallographic orientations align with applied stress. Slip systems tend to align with the shear direction to maximize the resolved shear stress [83,90]. In BCC  $\alpha$ -iron,  $\{110\}$  are the slip planes, and  $\langle 111 \rangle$  are the slip directions, so the  $\{110\}\langle 1\bar{1}1 \rangle$  slip systems are preferred. When shear is induced during plastic deformation, the resolved shear stress is maximized when the  $\{110\}$  lie parallel to the shear direction, like a deck of cards. This is why the  $\langle 110 \rangle \alpha$  wire texture is commonly found in HPT, wire drawing, and other deformation modes that induce high shear strains [63,78]. The SMAT process also induced nanocrystalline regions with grain sizes less than 10 nm, suggesting the formation of the  $\langle 110 \rangle \alpha$  wire texture is accompanied with the dissolution of  $\text{Fe}_3\text{C}$ .

The  $\{110\}$  // the surface texture was developed through dislocation slip and generation of geometrically necessary dislocations. At the same time, dislocation accumulation and interactions formed subgrain boundaries, which were eventually transformed to high angle grain boundaries, as is consistent with previous reports [10,11,13,40,64,65,88]. These defect structures serve not only to accommodate strain but also to orient the crystallographic directions towards the highest shear directions. The texture, however, is strongest only in the top 100  $\mu\text{m}$ , while grain refinement and shear strain accumulation are also prevalent at depths  $> 350 \mu\text{m}$ . In these regions, the lack of a strong shear direction may be the reason for the weakness of the texture. Cementite thinning and fragmentation may also play a role. It is clear, however, that the texture forms over a gradient, and is most strongly formed at the highest shear strains with the most severe grain refinement.

Because the gradient texture will locally affect deformation mechanics, it will likely play a role in the global deformation of the sample. For example, the texture gradient will lead to a deformation gradient, which causes macroscopic mechanical incompatibility that has been shown to increase mechanical strength and ductility simultaneously in similar systems [14–16]. Further investigation on the effects of gradient textures and their global response to mechanical stress could provide insight to the exciting developments in gradient structured materials.

### **3.6 Conclusions**

In summary, SMAT imparted very large shear strain near the sample surface, which decreases along the depth, which resulted in gradients in hardness, grain size and texture. Fe<sub>3</sub>C dissolution occurred near the surface, which helped with the reduction of grain size to 10 nm in local areas. {110} // SMAT texture was produced over a depth of 100 μm, below which the texture is complex. Further investigation on the effects of gradient textures and their global response to mechanical stress is needed to provide insight to the exciting developments in gradient structured materials.

## 4 Round Gradient Structures

### 4.1 Introduction

Metals exhibiting gradient microstructures have recently become the focus of research for their remarkable ability to produce a superior combination of strength and ductility in metallic systems [14–16]. These “gradient structures” often consist of nanocrystalline or ultrafine grains at the surface of a tensile sample, which gradually transition to coarse grains at the interior over distances of ~50 micrometers or longer. In addition to grain refinement, these gradient structures often possess high residual compressive stresses and texture gradients [35,86], which have been reported to improve wear resistance, fatigue life, and toughness [17,90–92]. Although the means by which gradient microstructures can be created include Surface Mechanical Grinding Treatment, Surface Mechanical Attrition Treatment (SMAT), Ultrasonic Shot Peening [93], Wire Brushing [94], and Air Blast Shot Peening [95], most of the seminal work was undertaken with SMAT [14,19,20,89,90,94]. Much like conventional shot peening, SMAT uses round balls to repeatedly impact the surface of a material. However, the number of impacts and the energy of impacts is often much greater, leading to surface grain refinement to the nanocrystalline regime.

Gradient structures synthesized by SMAT or other mechanisms are relatively well characterized, but their general effect on global mechanical response is poorly understood. For example, SMAT of IF Steel improved the yield strength by a factor of ~2.5 while the ductility was only reduced by ~15% [96]. However, SMAT of pure iron led to similar

strength improvements, though ductility was reduced by more than 50% [20]. In general, yield strength is universally improved in gradient structures, though it seems ductility can either decrease [20], remain more or less unchanged [15], or increase [14]. The discrepancy, in part, must be explained by the mechanism or mechanisms by which gradient structures deform and has been attributed to grain growth, dynamic hardening, strain partitioning, and dislocation accumulation at grain boundaries, to name a few [14,16,18,19,96]. One mechanism that has been experimentally verified is the evolution of a multi-axial stress state during tensile testing of the gradient structure [15]. The stress state evolution necessarily rises due to mechanical incompatibility of the hard surface layer and ductile core, and has been observed in flat gradient structures [15,16]. The net result of this interaction is that the applied 1D tensile stress is converted into a 2D stress state in flat gradient structures during uniaxial tensile deformation. However, in round samples, the ductile core is fully confined by the hard shell and unable to contract in the early tension stage like flat samples due to the lack of freestanding directions. This should lead to a more complex stress state upon loading and could have a greater strengthening effect compared to flat samples [23].

Here we report that gradient structured aluminum rods processed with SMAT have strength that is twice as high as what is predicted by the rule of mixtures, which is dramatically higher than the synergetic strengthening observed in gradient-structured flat samples [15]. To probe the mechanisms behind this surprising observation, the gradient structures of round samples are characterized and the texture evolution was studied with EBSD to explore the stress state evolution during tensile testing.

## 4.2 Experimental Procedure

1350 Al wire was used for this study and was machined into tensile specimens with a gauge diameter of 5 mm and a gauge length of 20 mm. The samples were annealed (O tempered) at 370°C for 21 hours under vacuum to produce homogenized, coarse grains. This annealing also produced a recrystallized cube texture, which was confirmed with Electron Back Scattered Diffraction (EBSD). The SMAT treatment was conducted using a modified SPEX Mill for 5 minutes using 7 stainless steel balls 6 mm in diameter. By nature of the randomized impacts, the tensile sample was free to rotate in the vial and exhibited uniform deformation across the gauged section. The resulting “as SMAT” sample was cross sectioned and prepared for imaging by conventional polishing techniques and ion milling for 45 minutes. EBSD data was acquired with an Oxford EBSD detector installed in the dual Beam FEI Quanta 3D FEG. Microhardness testing was conducted on the ion polished surface using a Mitutoyo Model HM-11 with a Vickers diamond indenter at a load of 0.001 N. An average of 10 indentations was used for the microhardness profile and Kikuchi patterns from EBSD revealed the prepared sample was free from polishing damage. The figure below the gradient structure produced by the SMAT surface, the tensile test results, and the resulting hardness profile from surface to interior.

## 4.3 Tensile Properties

As can be seen in the figure below, the O tempered aluminum exhibited a yield strength of 27 MPa which is dramatically increased to 59 MPa after SMAT treatment. Examining the cross section of the as-SMAT sample, it is clear that a deformation gradient,

characterized by dislocation accumulation and subgrain boundaries, extends to a depth of  $\sim 250 \mu\text{m}$  from the surface. However, the microhardness results show that the hardened layer extends to a depth of  $600 \mu\text{m}$  from the surface, and the hardness of the surface layer is only improved by  $\sim 50\%$ . In order to surmise the effect of the hardened surface layer, rule of mixtures estimations were calculated using hardness data and the volume fraction of each hardened layer, shown to scale below. This rule of mixtures analysis has been successfully used in other gradient samples to further reveal the hardening effect of the surface layer [14,19].

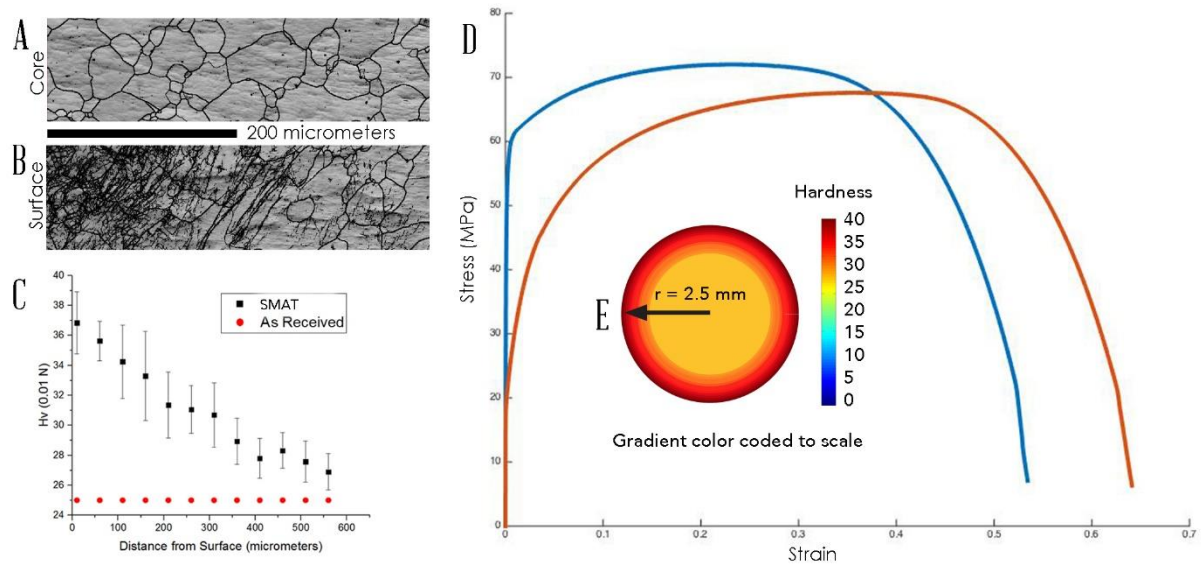


Figure 4.1 (a) EBSD map of the O tempered aluminum and (b) after SMAT processing. (c) Microhardness profile at various depths and (d) Tensile test results of the SMAT and as-annealed samples with arrow indicating the rule of mixtures prediction of yield strength. (e)

Color coded hardness map showing depth of the gradient to scale.

#### 4.4 Relationship between Hardness and Yield Strength

There is some debate in the community regarding the relationship between microhardness, yield strength, and ultimate tensile strength. The initial construction by Tabor predicted yield strength in the absence of strain hardening, and found the commonly used empirical relationship,  $3\sigma_y = H_v$  [97]. When including the effects of strain hardening for soft aluminum alloys, various models have been proposed, but the raw data in these studies deviates very little from a linear relationship [98,99]. However, because the indenter used in microhardness testing induces plastic flow, there is also a relationship that has been reported between microhardness testing and ultimate tensile strength [97,100,101]. However, most of these relationships were constructed with steels, which show very little variation between yield strength and ultimate tensile strength at any hardness condition. There is some discrepancy for metals with very high strength and low ductility, as early onset of necking causes the ultimate strength – hardness linear relationship to deviate. So clearly there have been predictions for both tensile and yield strength as a function of microhardness. In order to surmise this relationship for aluminum, a literature survey was conducted of low alloyed aluminum, to investigate reported hardness strength relationships. In addition, there is also strong experimental evidence corroborating the linear relationship between microhardness and yield strength in 1000 series aluminum [99,101–105]. Lastly, although there is a linear relationship between hardness and ultimate strength for aluminum, this relationship deviates at low hardness values, where the trend shows lower predicted ultimate tensile strengths.

Therefore, there is strong evidence to suggest that hardness and yield strength are proportional for low strength, low alloyed aluminum.

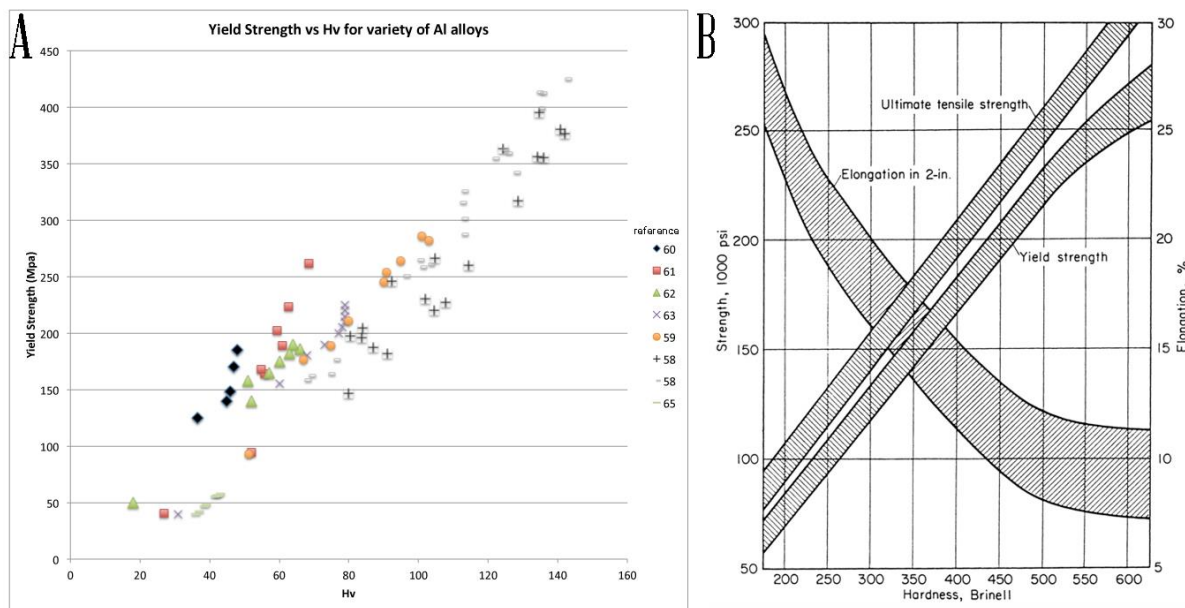


Figure 4.2 (a) Literature survey of hardness and yield strength results reported for low alloy aluminum. (b) Cartoon showing relationship between tensile properties and hardness for steels.

#### 4.5 Rule of Mixtures Prediction

Given the apparent linear relationship between yield strength and microhardness in 1000 series aluminum alloys, the microhardness data obtained across the gradient structure can be used to predict the yield strength of each layer within the gradient. It can be assumed that yield strength and microhardness measurements are proportional such that

$$\sigma_y \sim Hv$$

Therefore, rule of mixtures predictions can be written as follows:

$$\frac{\sigma_{gs}}{\sigma_{cg}} \sim \frac{\sum V_f H_{gs}}{H_{cg}}$$

where  $\sigma_{gs}$  is the yield strength of the gradient structured rod,  $\sigma_{cg}$  is the yield strength of the coarse grained O tempered rod,  $H_{gs}$  is the hardness of each layer in the gradient and its respective volume fraction,  $V_f$ , and  $H_{cg}$  is the hardness of the coarse grained O tempered rod.

Examining the data, we see that

$$\frac{\sigma_{gs}}{\sigma_{cg}} = 2.2; \quad \frac{\sum V_f H_{gs}}{H_{cg}} = 1.1$$

Therefore, there is significant strengthening that is not accounted for by rule of mixtures predictions. In fact, the strengthening contribution of each layer appears to account for very little improved strength in the gradient structure itself.

#### 4.6 Microstructural Analysis

To examine possible strengthening mechanisms at hand, the SMAT-produced microstructure gradient was characterized in cross section using EBSD. Below are various maps of the aluminum sample and the inverse pole figures of local areas. Typical deformation structures in aluminum can be seen at various depths, including subgrain boundaries, slip bands, and dislocation cells. Although the grain size has not been reduced to the nanocrystalline regime, magnification of the surface shows the subgrain boundary size approaches  $\sim 3 \mu\text{m}$ . These subgrain boundaries are typical of the early stages of SMAT processing, and have been observed in samples subjected to small revolutions of High Pressure Torsion (HPT) [90,106]. However, the degree of grain refinement is quite mild at the surface of the SMAT sample which correlates well to the mild improvement in hardness at the surface, as seen in the figure below.

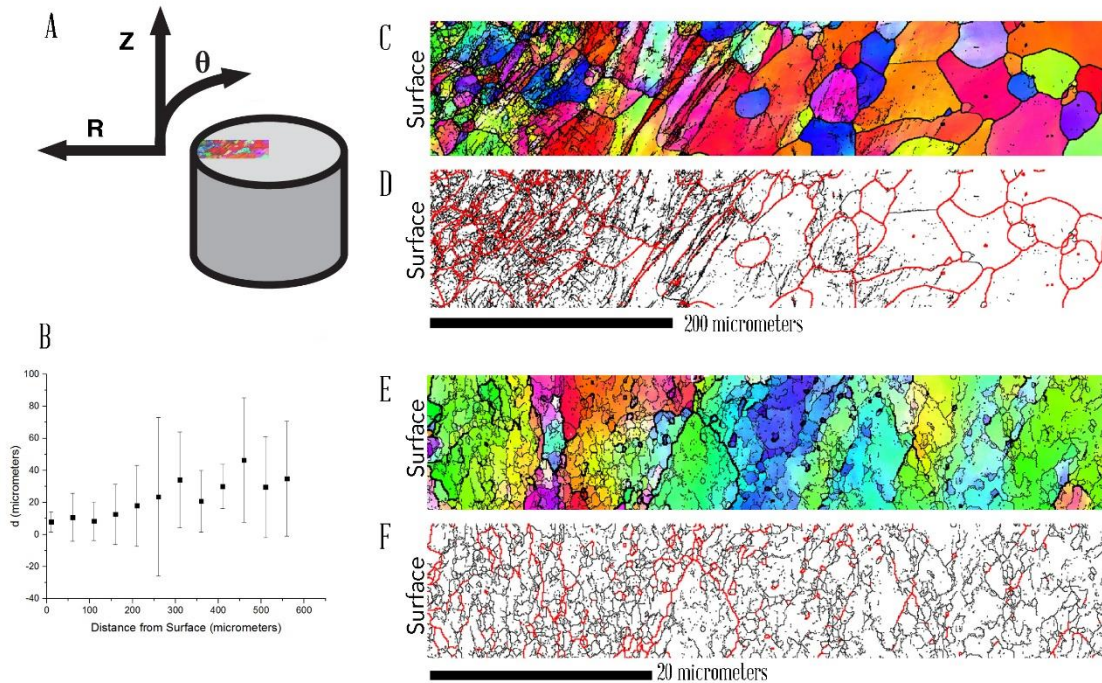


Figure 4.3 (a) Convention used for axis of the round SMAT sample along the surface normal (R), tensile direction (Z), and radial direction ( $\theta$ ). (b) Grain size gradient. (c and d) EBSD map of the SMAT sample projected along Z and grain boundary map, respectively. For the grain boundary maps, red lines indicate misorientation of  $>10^\circ$  and the black lines indicate misorientations  $>2^\circ$ . (e and f) High resolution EBSD map of the very top surface layer showing numerous subgrain boundaries when projected along Z and its grain boundary map, respectively.

Beyond the microstructure, there could be other mechanisms that improve the strength of the SMAT sample. It is well known that SMAT samples exhibit high compressive residual stresses, and can develop multiaxial stress states in tension [36,107]. In fact,

strengthening from both the initial stress state and the stress state evolution would not be accounted for in the rule of mixture predictions since this model neglects transverse stresses and interaction between layers within the gradient. It is well known that the compressive residual stresses in SMAT structures can exceed the yield strength of the coarse grained core by a factor of 3 and extend to depths of nearly 1 mm [36,108]. In shot peening, similar compressive stresses were shown to increase the yield strength of samples by  $\sim 2x$  and therefore some of the hardening beyond rule of mixtures can be accounted for by this phenomenon [35]. In some cases, 40% of the strengthening of gradient structures has been attributed to this residual stress [67]. In addition to this effect, the multiaxial stress evolution, which arises from the different Poisson's ratios between early-plastic and stable elastic regions, should also contribute to strengthening [16]. At low strains, the stress applied will exceed the yield strength of the coarse grained region, inducing plastic deformation while the surface is still deforming elastically. As the inner region attempts to contract, the surface must develop a compressive stress to remain coherent with the shrinking interior, and this phenomenon has been observed experimentally in flat samples [15,16]. In round samples, however, the gradient confines the interior layer, creating 3D internal stresses. Direct observation of the strain accumulation within the gradient is not possible with round samples as with flat samples. Using EBSD, it is possible to get clues about the deformation mechanism of the gradient structure by examining the post-mortem microstructure of the SMAT sample.

#### 4.7 Post-Mortem Analysis

In order to investigate the stress state evolution of the gradient layer, samples were taken from the post-mortem “as annealed” and SMAT samples from the uniformly elongated region to compare the microstructure using EBSD. Because the texture symmetry depends on the deformation symmetry, the texture evolution gives insight to the stresses evolved during yielding. If out of plane stresses are operating on the gradient, then the symmetry of these stresses should be evident in the pole figures. After tensile testing, the post-mortem EBSD maps clearly differed, and the Z and  $\theta$   $\{111\}$  and  $\{110\}$  axis projection pole figures of the top layer of both samples showed a similar symmetry but the SMAT sample showed out of plane texture symmetry.

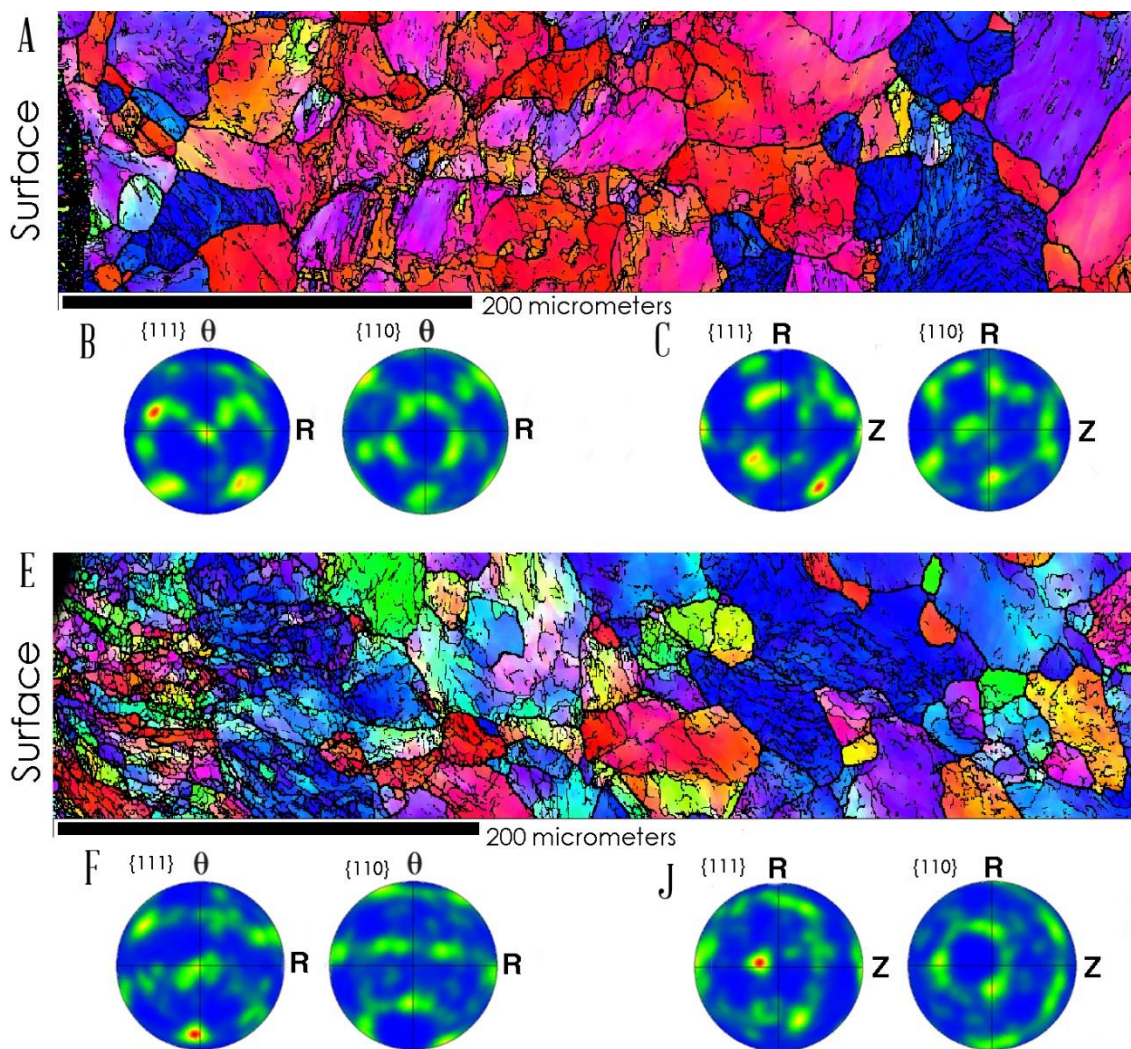


Figure 4.4 (a) Z projection EBSD map of the uniformly elongated “as annealed” sample after tensile testing and corresponding pole figures showing (b) Symmetric smearing of  $\{110\}$  about the tensile (Z) axis and c)  $\theta$  axis projection. e) Z projection EBSD map of the uniformly elongated SMAT sample after tensile testing and corresponding pole figures projected along c) the Z axis and d) the  $\theta$  axis. There is a clear symmetry that develops along the  $\theta$  axis in the post mortem SMAT sample not present conventional samples.

In the as-annealed sample, the Z projection pole figure shows some {111} character, and some symmetric "smearing" of the {110} about the tensile (Z) axis, all of which is the common texture seen in uniaxial drawing of aluminum [40–42]. Interestingly, the pole figures from the SMAT sample show a similar symmetry, but not around the tensile axis. It is clear from the pole figures that the  $\theta$  direction develops a similar wire texture to Z direction of the as annealed sample. This out of plane texture is evidence that a multiaxial stress state evolves during tensile testing that is not present in samples lacking gradient structures.

#### 4.8 Conclusions

Despite the evidence of out of multiaxial stress state evolution, it is very difficult to discern the primary strengthening mechanism of this gradient structured aluminum alloy. It was not possible to quantify the residual compression, which has been shown in some cases to greatly affect mechanical performance [35,67]. In addition, the effect of residual stresses on the microhardness testing could skew the hardness due to the compression at the surface and tension in the core. Also, although the linear relationship between hardness and yield strength was used to predict rule of mixtures calculations in this study, the high rate of strain hardening in aluminum could introduce error into this prediction especially in the measurements of the ductile core. Further studies should explore these confounding effects in more detail to elucidate the strengthening mechanisms in gradient structured aluminum rod.

In conclusion, aluminum treated by SMAT exhibits a yield strength far beyond what is predicted by rule of mixtures. The gradient structure produced by SMAT produced some improvement in hardness and EBSD maps showed the hardening is accompanied by dislocation accumulation, subgrain boundaries, and very little grain refinement. EBSD of the post-mortem samples showed that the gradient structured aluminum developed an out of plane texture that indicates a complex, multiaxial stress evolution during tensile testing that is not present in its coarse grained counterpart.

Unlike previous reports of gradient structures where increased strength and ductility were attributed to grain growth, dislocation accumulation at grain boundaries, and other mechanisms, this report provides evidence that strengthening in round SMAT samples is due to both the complex initial stress state of the material as well as the dynamic strain hardening that occurs within the mismatched layers, which produced 3D complex stress states. These effects lead to synergetic strengthening far beyond of what is predicted by the rule of mixtures in gradient structured rod. Further investigation of the residual stress effect and stress state evolution in gradient structures should shed light on the magnitude of contributions by these strengthening mechanisms.

## 5 Strain Analysis in Gradient Structured Rod

### 5.1 Introduction

Due to the limited number of samples available for testing in Chapter 4, a follow up study was conducted to investigate the evolution of the gradient structure during tensile testing. Although there was evidence supporting non-uniform multiaxial stress state development in the 1350 SMAT sample, the magnitude of this effect was unknown. In addition, the residual stresses in the SMAT layer that are known to effect tensile strength and plasticity could not be quantified. In SMATed Ni, the residual compression reached a maximum of 1200 MPa, nearly 3x the yield strength of the starting material [32,33]. As a result, up to 40% of the yield strength enhancement was contributed to residual stresses, with the other 60% coming from grain refinement and cold work within the gradient [30]. Other reports have also shown that the magnitude of the residual stress can be several times the yield strength of the base material, but very few studies have examined its effect on tensile plasticity within the gradient [33,35]. In addition, the contribution of the evolution of multiaxial stresses to strength and ductility has not been quantified. Some computational modeling has been conducted, but no experimental studies have been conducted to examine this effect [15,30,109]. Lastly, the softening of the hardened surface layer has been a proposed mechanism that improves plasticity, though experimental evidence of this phenomenon has mainly been limited to the necked region [22]. Therefore, the objective of this experiment is to investigate the evolution of the microstructure, residual stress, and hardness of gradient structured aluminum rod loaded under tension.

## 5.2 Experimental Procedure

The alloy used for this study was 5005 aluminum, as specified by ASTM B209 with composition 0.3 Si, 0.7Fe, 0.2 Cu, 0.2 Mn, 0.5-1.1 Mg, 0.1 Cr, 0.25 Zn and balance Al. The alloy was chosen so that no second phases would be present in the gradient structure. The Al rods were machined into tensile samples with three different diameters; 6mm, 5mm, and 4mm. All samples had the same gauge length of 28 mm, and were O-tempered (650°F for 3 hours) before the SMAT process. Samples were processed in the modified SPEX mill described earlier for either 5 or 15 minutes using 10, ¼” SS balls. Tensile testing was conducted using a MTS Landmark with extensometer and at a strain rate of  $5 \times 10^{-4}$ . The diameter used for stress calculations was taken as the lowest of 6 readings on digital calipers for each sample and triplicate samples were tested at each condition. A set of 6mm diameter samples processed for 5 minutes were prematurely unloaded at 0.8%, 3.7%, and 16.7% strain in order to investigate the microstructure at various strains.

Microstructural analysis was conducted by copper plating samples using a conventional electroplating solution, followed by grinding with lapping films and a thorough polish with 1 $\mu$ m diamond suspension for 2 hours. Final polishing The resulting “as SMAT” sample was cross sectioned and prepared for imaging by conventional polishing techniques and ion milling for 1 hour in a Fischione Ion Mill (Model-1060) at 5kV, 75% focus, and 5° tilt. EBSD data was acquired with an Oxford EBSD detector installed in the dual Beam FEI Quanta 3D FEG at 8x8 binning for standard imaging, and 1x1 binning (full resolution) for

strain analysis. Microhardness testing was conducted on the ion polished surface using a Mitutoyo Model HM-11 with a Vickers diamond indenter at a load of 0.0025 N. An average of 10 indentations was used for the microhardness profile and Kikuchi patterns from EBSD revealed the prepared sample was free from polishing damage. EBSD Texture analysis revealed that after tempering, the samples had a strong wire texture in the tensile direction with pronounced  $\{100\}$  and  $\{111\}$  character, typical for recrystallized aluminum [40,110].

EBSD mapping of the top 100  $\mu\text{m}$  of both the 15 and 5 minute SMAT processing revealed a reduction in grain size at the surface accompanied by a gradual shearing of the surface grains. This morphology is similar to low carbon steel microstructures presented earlier where the SMAT surface was shown to exhibit high shear strains [86]. Additionally, the microstructures of both samples show a transition in the wire texture at the surface, where the smaller grains show a broader distribution of orientations. The grain boundary maps show the 15 minute SMAT treatment developed more subgrain boundaries and low angle GB relative to the 5 minute sample.

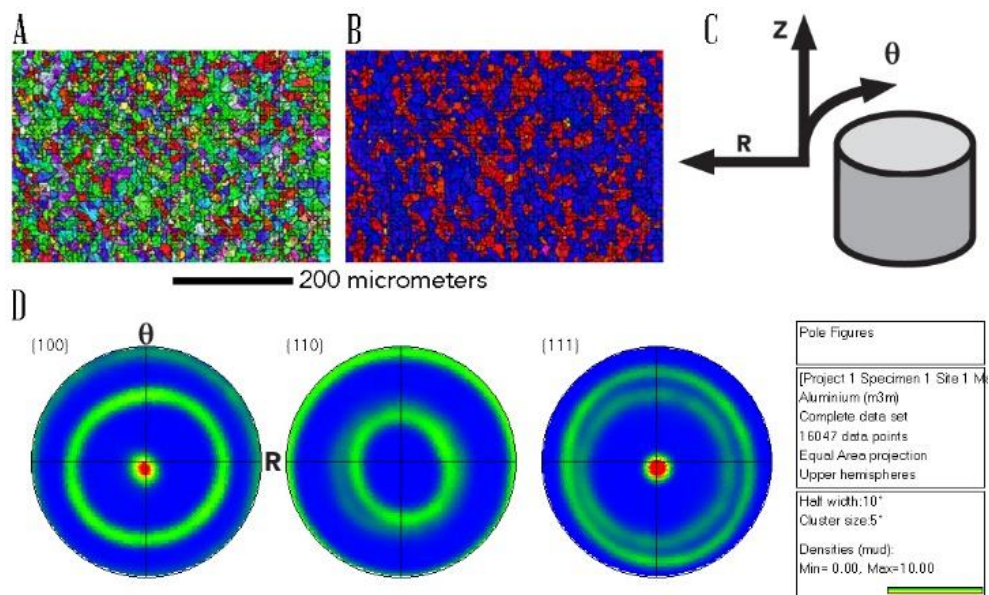


Figure 5.1 (a,b)  $\theta$  and Z projection IPF maps, as defined by (c) of the as-annealed interior in the 5005 rod. (d) Z projected pole figure of the as-annealed 5005 rod showing a strong recrystallized wire texture.

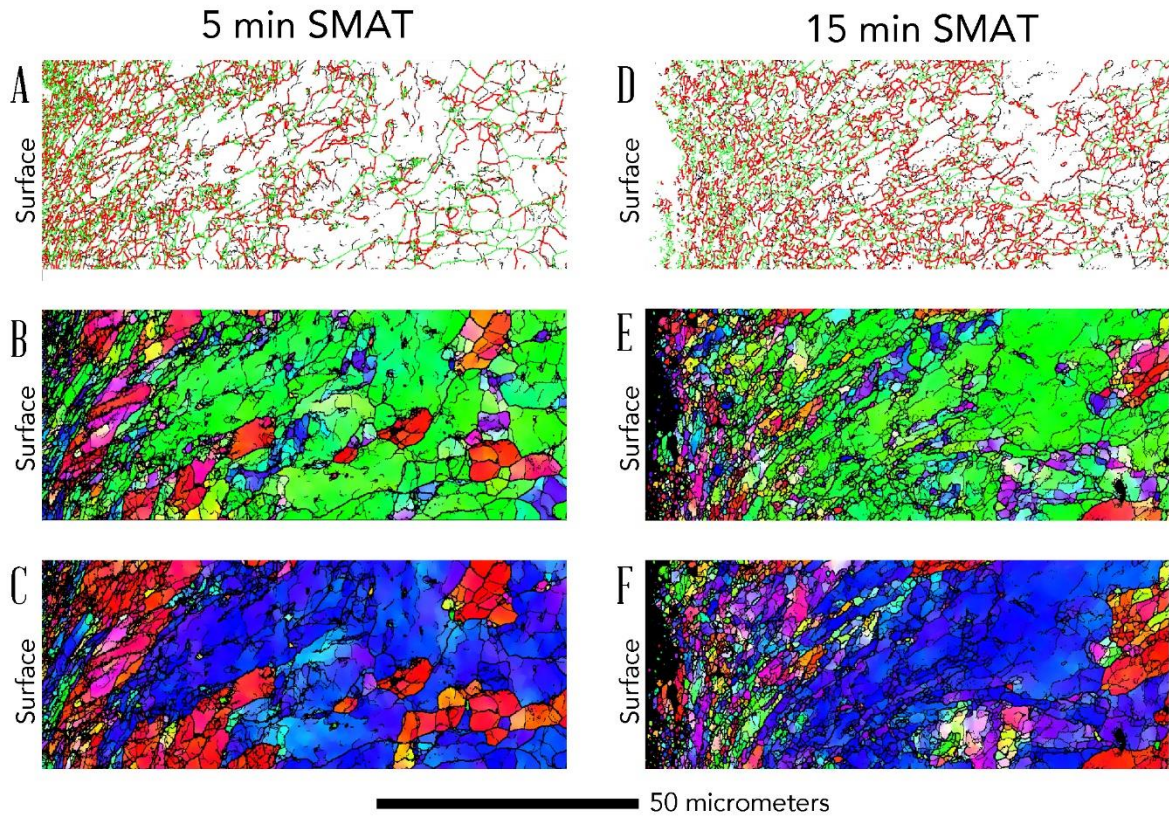


Figure 5.2 EBSD map of the 6mm rod sample SMATed for 5 minutes (a-c) and for 15 minutes (d-f). (a,d) Grain boundary maps showing subgrain boundaries ( $>2^\circ$ ), low angle GB ( $>10^\circ$ ), and high angle GB ( $>15^\circ$ ). (b-e) the  $\theta$  projection IPF coloring and (c-f) the Z projection

### 5.3 Tensile Results

Tensile tests reveal that the SMAT layer has improved the yield strength, ultimate tensile strength, and total elongation to failure in nearly all samples. Here the total elongation to failure is defined as the strain at which the load is reduced 100N from the load at the ultimate tensile strength. As expected, the 6 mm samples exhibited the lowest volume

fraction of the SMAT layer, and exhibited lower strength and higher ductility relative to the other samples. However, there is very little variation between the tensile properties for the 4mm and 5mm samples at all processing conditions. Surprisingly, there were very little differences in tensile properties for all samples processed for 5 minute and 15 minute SMAT times. The uniform elongation, however, appeared to be adversely affected by longer processing times, and was reduced in all samples relative to the O-tempered control.

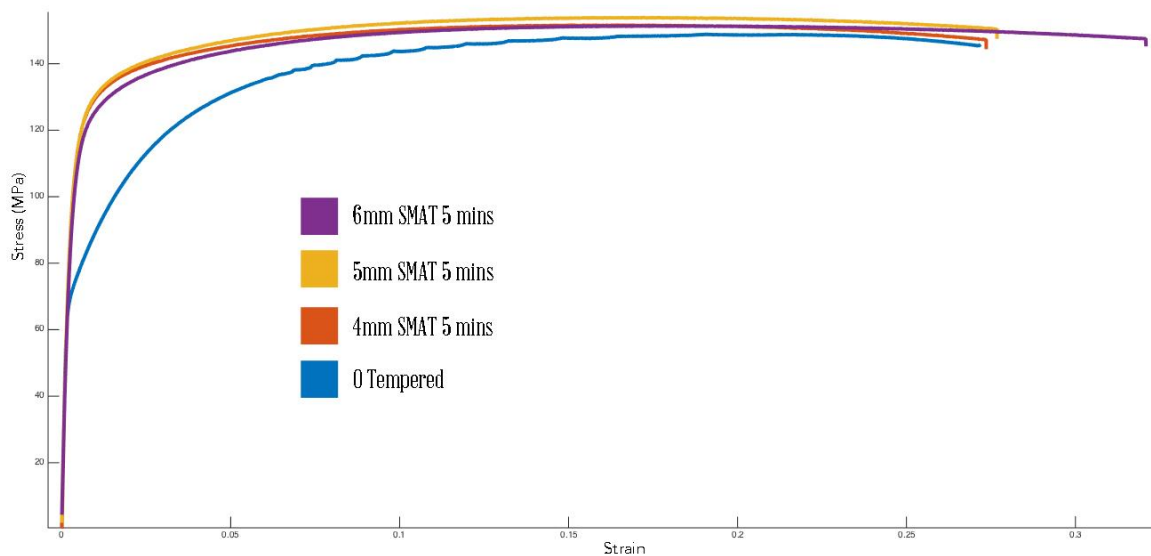


Figure 5.3 Engineering stress-strain curve plotted for the 4, 5, and 6 mm SMAT samples processed for 5 minutes compared to the O tempered state.

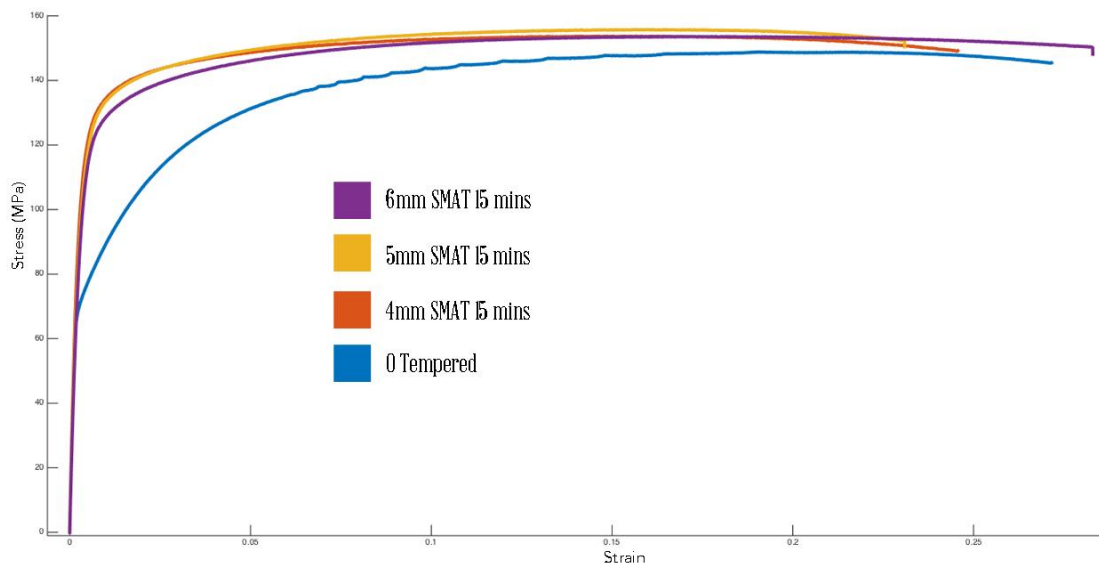


Figure 5.4 Engineering stress-strain curve plotted for the 4, 5, and 6 mm SMAT samples processed for 15 minutes compared to the o tempered state.

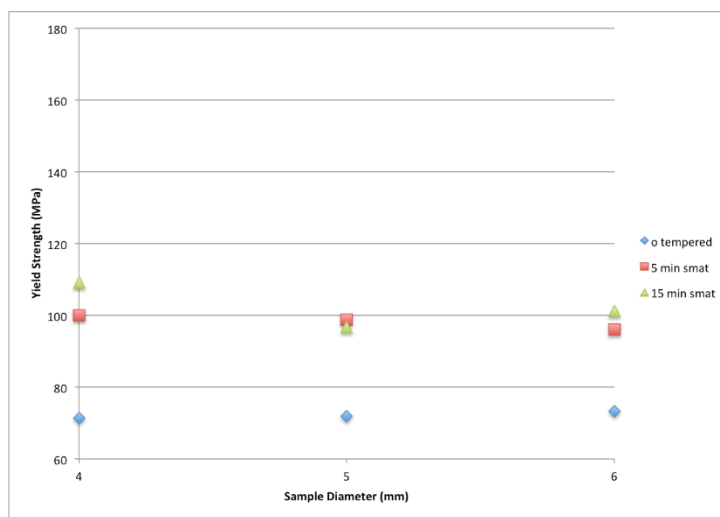


Figure 5.5 Average yield strength for each diameter and processing condition.

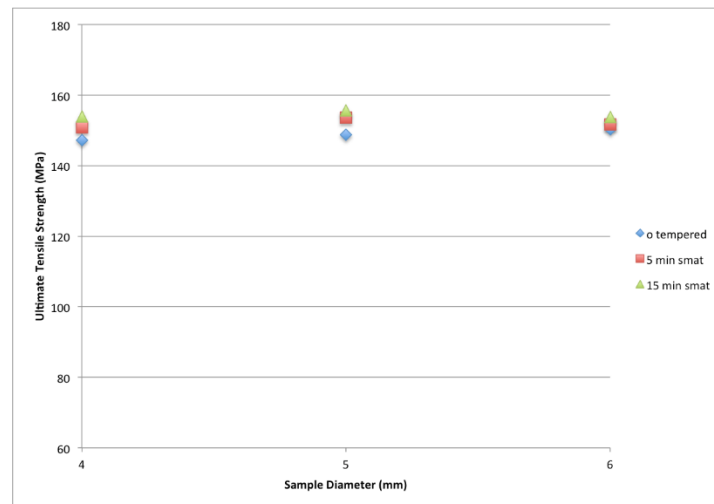


Figure 5.6 Average ultimate tensile strength for each diameter and processing condition.

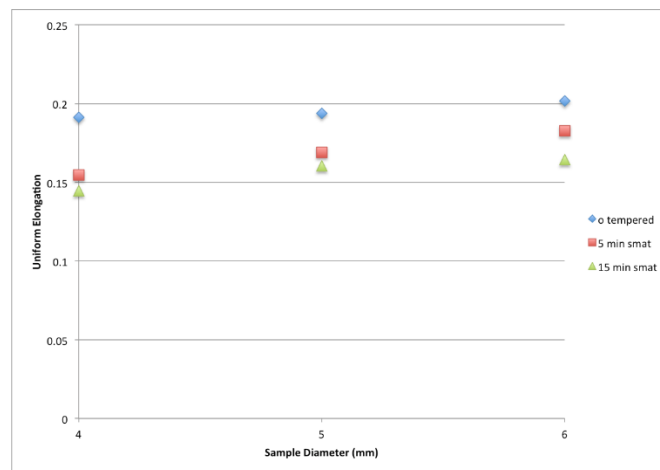


Figure 5.7 Average uniform elongation for each diameter and processing condition.

To investigate the phenomenon behind this extraordinary strengthening, cross sectional samples at various strains were imaged using EBSD. First, the “as SMAT” sample was imaged to discern the scan parameters needed for other samples. Although 1350 and 5005 aluminum alloys have similar mechanical properties, the SMAT microstructure is noticeably different between the two. Figure 5.7 shows the 0% strain SMAT microstructure grain boundary map along with other cross sections at discrete strains. Immediately apparent is the high density of low angle ( $>10^\circ$ ) grain boundaries at the surface of the gradient. This region exhibits grain sizes in the UFG regime, but the average size was not less than 500nm. As the gradient begins to undergo plastic deformation at  $\epsilon = 0.8\%$ , It appears that some low angle grain boundaries begin converting to high angle ( $>15^\circ$ ) grain boundaries, and that the depth of the grain refined region becomes slightly larger. At  $\epsilon = 3.7\%$  more high angle grain boundaries are found at the top surface, and at  $\epsilon = 16.7\%$ , the slight deepening of the grain refined region continues. However, this apparent change in grain boundary size was not statistically significant, so very little conclusions could be made on grain boundary maps alone.

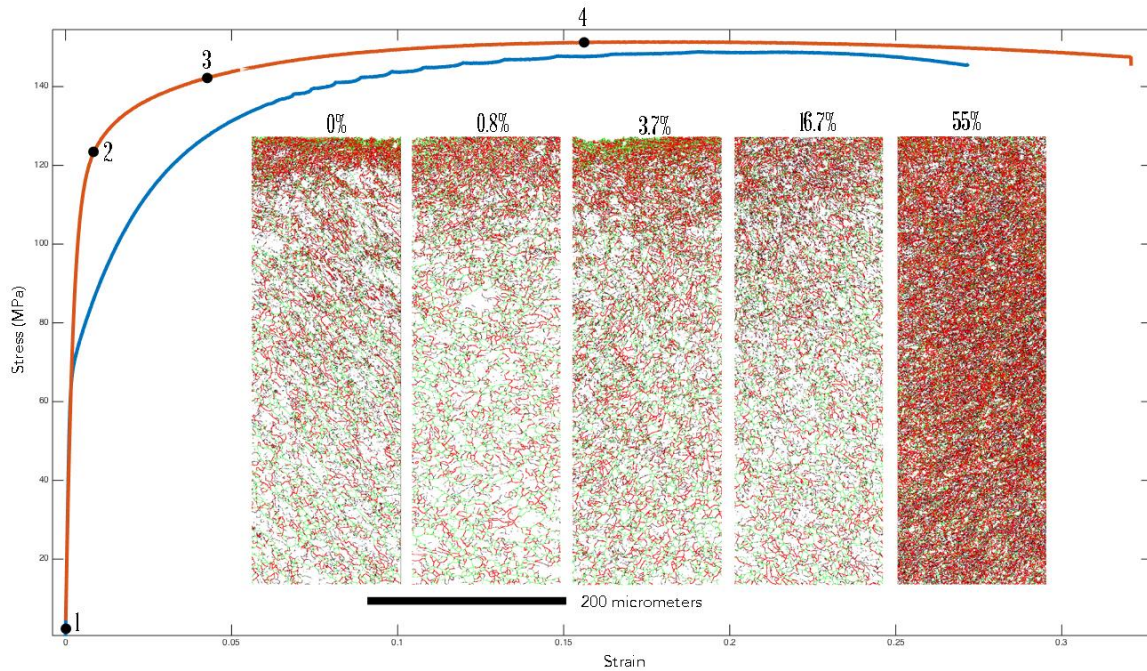


Figure 5.8 Tensile test and corresponding EBSD maps of 6mm samples SMATed for 5 minutes unloaded at various strains where the red curve is the gradient structure and the blue curve represents the o tempered tensile results. Grain boundary maps are colored black for subgrain boundaries ( $>2^\circ$ ), red for low angle grain boundaries ( $>10^\circ$ ), and green for high angle grain boundaries ( $>15^\circ$ ).

In addition to cross sectional EBSD mapping, microhardness testing was utilized to investigate the mechanical properties at the same strains the EBSD mapping were conducted. At first glance, the hardness profile revealed similar properties to general SMAT gradient structures. However, at 0.8% strain, the hardness is reduced along the top 800 micrometers of the gradient, which is surprising considering the sample was more strained than the as-SMAT sample. At higher strains, the hardness profile increases in intensity uniformly. In the

uniformly elongated region, another interesting phenomenon is observed as the interior appears to harden asymmetrically with respect to the surface. In this region, the interior hardness rises faster than the surface, until necking where the gradient and interior both become harder. Clearly, there complex hardening behavior occurring within the gradient, which cannot be conclusively determined by microhardness testing alone.

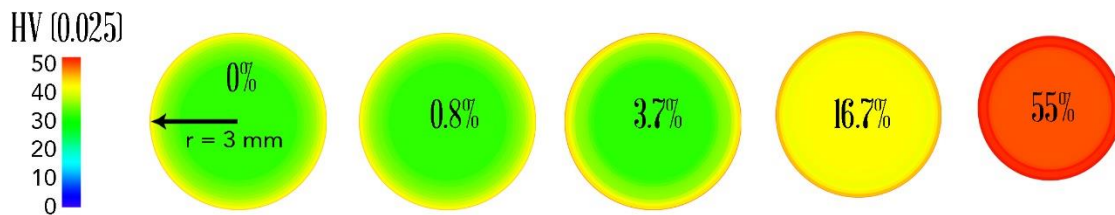
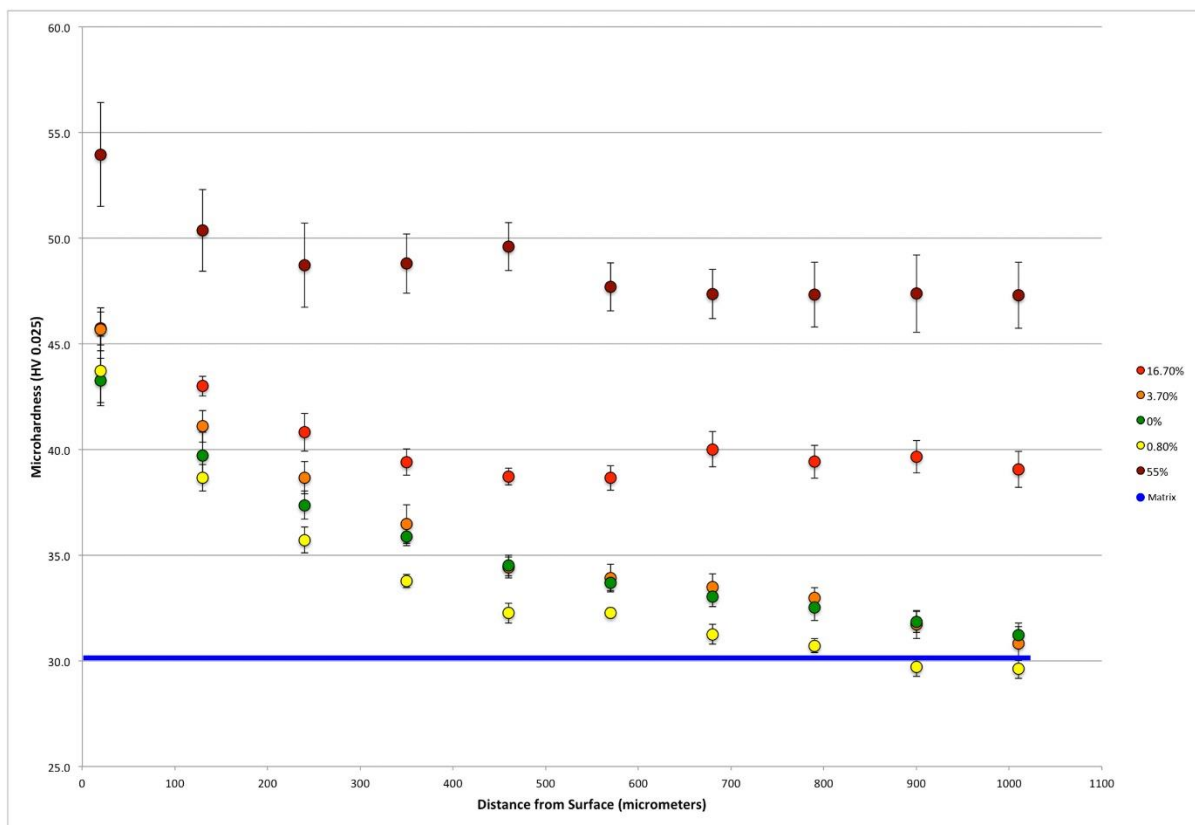


Figure 5.9 Microhardness testing of the gradient structure showing profiles at various strains.

Inset shows gradient hardness and volume fraction to scale.

#### 5.4 GND Density Evolution

Using the EBSD data collected from the maps above, a kernel averaging approach was utilized to calculate the misorientation, or curvature within each grain. Because the lattice curvature is directly proportional to the GND density, variations in misorientation could provide clues to deformation mechanism underlying the high strength of these samples [69,74,76,111]. Therefore, evolutions in average misorientation within scanned regions should be a good estimate for GND evolution. For the analysis, a 3x3 region within each grain was used via the kernel averaging approach in order to calculate the relative curvature of the lattice. Data was acquired with a step size of 250 nm, and no data cleaning was used to approximate regions not indexed. The average misorientation was calculated at every 20  $\mu\text{m}$ , and were plotted accordingly. As a reference, a map of the coarse grained interior prior to SMAT treatment was collected to serve as the unstrained region. Immediately noticeable is the clear accumulation of GNDs approaching the SMAT surface for all samples. However, the evolution of GND density is not very clear. At  $\epsilon = 0.8\%$ , the GND density is reduced within the gradient, and possesses less GNDs than the coarse grained interior at a depth of 200  $\mu\text{m}$ . Interestingly, this phenomenon corresponds extremely well with the reduction in microhardness observed in the same sample. Since both GND density reduction and microhardness reductions were seen at the same strain, this discrepancy cannot be dismissed. However, as the load increases, the GND density rises again, and stays more or less constant up to  $\epsilon = 16.7\%$  until necking where a new GND density profile emerges.

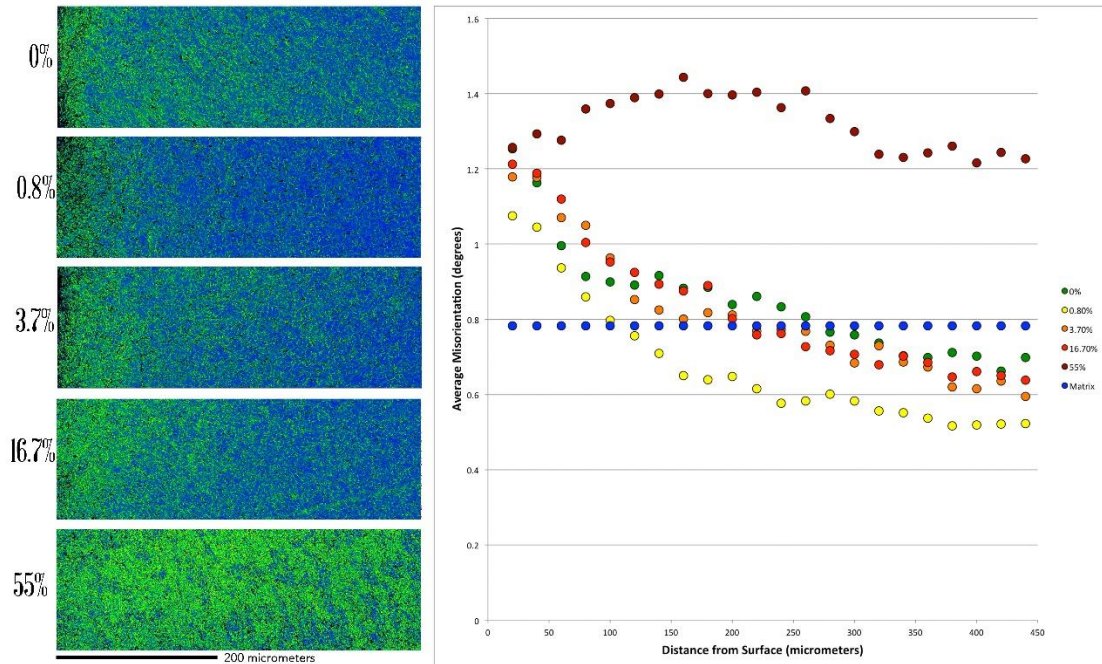


Figure 5.10 Misorientation plots for 6mm samples unloaded at various strains. The plot shows an initial reduction in GND density which then rises with increased tensile strain.

## 5.5 EBSD Strain Analysis

In order to acquire high resolution Kikuchi patterns for strain analysis, the beam current was brought to 45nA and the binning was reduced to 1x1, full resolution patterns. First, simple scans of the surface and interior were compiled to examine whether the strain at the surface had an impact on the pattern quality. As expected, the Kikuchi bands were more

blurred and exhibited slight shifting at the surface relative to patterns collected in the undeformed matrix.

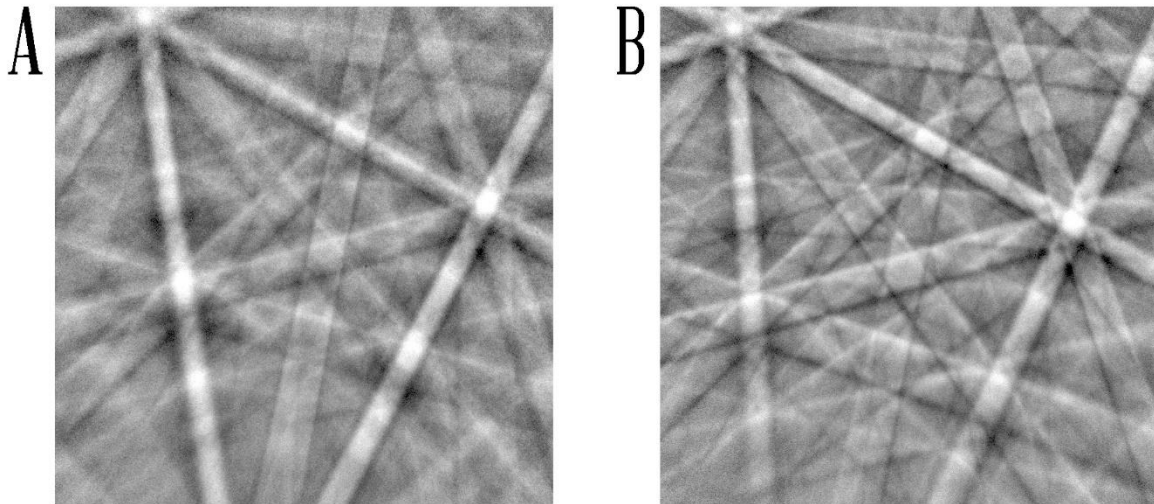


Figure 5.11 (a) Full resolution Kikuchi pattern collected 50  $\mu\text{m}$  below the as SMAT surface showing clear evidence of plastic deformation relative to the same Kikuchi orientation collected (b) in the undeformed core.

Once the microscope was optimized for this type of acquisition, a 40  $\mu\text{m}$  x 40  $\mu\text{m}$  scan of the interior region was collected with a step size of 1  $\mu\text{m}$ . Typically, step sizes on the order of 100-300 nm are preferred due to the noise that develops in the analysis for larger step sizes. However, once the mapped region was collected, the data was analyzed with commercially available software [57,58]. The Euler angles were used to run cross correlation of the collected patterns with a simulated Kikuchi pattern and the resulting strain maps are generated. Unfortunately, an indexing error arising from pattern centering calibrations caused

certain grains to not be analyzed correctly. It appears that the  $\{100\}$ //Z grains were successfully detected by the software, and the strain contour shows the slight lattice rotations within certain grains. In fact, the central grain exhibits close to zero strain along the shear strain components,  $\epsilon_{12}$  and  $\epsilon_{23}$ . Meanwhile, the hydrostatic components  $\epsilon_{11}$  and  $\epsilon_{22}$  indicate compressive and tensile strains are present that do not affect  $\epsilon_{33}$ .

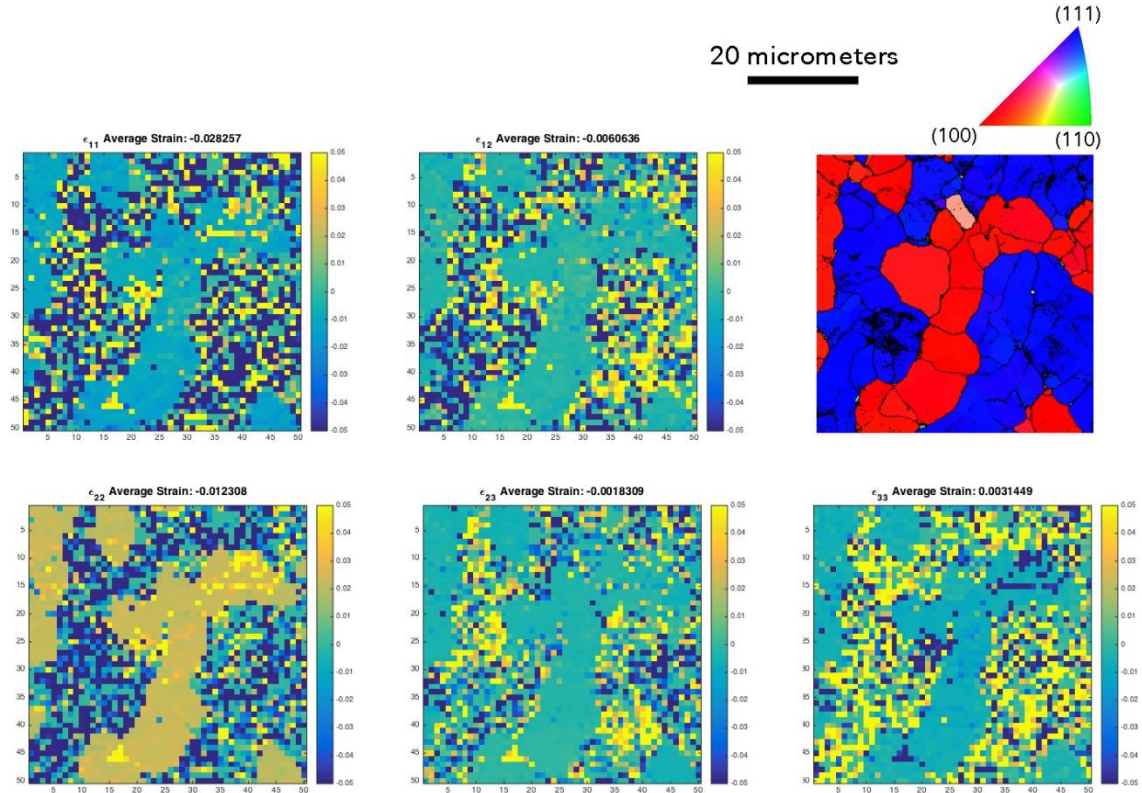


Figure 5.12 Partial reconstruction of the strain tensor using collected Kikuchi patterns in the undeformed matrix of the SMAT sample.

## 5.6 XRD Strain Analysis

Conventionally, XRD is used to characterize residual stresses in metallic samples, due to its high angular resolution [33,112,113]. Because the wavelength of x-rays is on the order of several angstroms, the x-rays are diffracted periodically at well-defined Bragg angles, as defined by Bragg's law.

$$\lambda = 2d^{hkl} \sin \theta^{hkl}$$

Where  $\lambda$  is the wavelength of the radiation source,  $d^{hkl}$  is the lattice spacing of planes with Laue indices h,k,l and  $\theta^{hkl}$  is the diffraction angle. In a perfect crystal, there would be no stress, so the diffracted peaks would correspond exactly to the Bragg angles. However, in the presence of an elastic stress, the  $d^{hkl}$  will be shifted as the atomic spacing changes to accommodate elastic strain. This shift can be used to calculate the strain in a given hkl plane by

$$\varepsilon^{hkl} = \frac{d^{hkl} - d_0^{hkl}}{d_0^{hkl}}$$

Where  $\varepsilon^{hkl}$  is the strain of a given hkl along the direction of the diffracted beam,  $d^{hkl}$  is the measured interplanar spacing, and  $d_0^{hkl}$  is the strain free lattice spacing. Although it is possible to reconstruct the entire strain tensor by calculating  $\varepsilon^{hkl}$  at 6 different Euler angles, the calculation of the in-plane stresses is more trivial. In this case, only the principal stresses are used since  $\sigma_{11} = \sigma_{22}$ ,  $\sigma_{33} = 0$ . Therefore, the compressive and tensile stresses can be calculated using

$$\sigma_{11} = -\frac{E_{hkl}\varepsilon_{33}}{2\nu_{hkl}}$$

Where  $\sigma_{11}$  is the principal stress for a calculated in-plane strain  $\epsilon_{33}$ ,  $E_{hkl}$  is the elastic modulus, and  $\nu_{hkl}$  is the Poisson's ratio.

Utilizing this technique, the residual stress was calculated at the surface of the 6mm sample SMATed for 5 minutes using Cu K- $\alpha$  x-rays. The theoretical peak positions were used for the unstrained  $d^{hkl}$  and peak shifts were acquired for the 311, and 222 planes, corresponding to stresses of 13.02 and 9.9 MPa-8 respectively 4.9, -93.3 MPa, respectively. Therefore the average residual compression at the surface of the 5 minute SMATed sample was calculated to be 89.9 MPa, which is higher than the yield stress of the O-tempered condition. Although the stress profile was not created for the various tensile strains listed earlier, it is assumed that the stress state evolution will occur similar to the Finite Element Modeling presented in chapter 2.

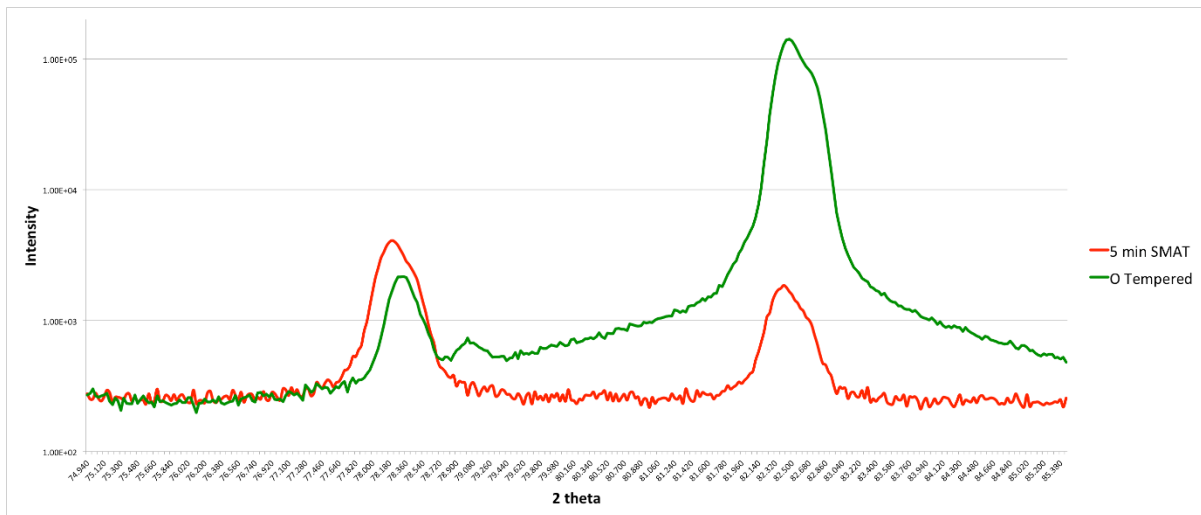


Figure 5.13 XRD Analysis of 5 minutes SMAT and O-tempered 6mm rod. The peak shifts correspond to lattice strain which indicates residual compression at the surface of the SMAT sample. The relative intensity variations arise from the texture differences in the two samples.

Interestingly, the residual compression at the surface,  $\sigma_s^{\text{rc}}$  has been strongly correlated with material yield strength  $\sigma_y$  for shot peened materials [35]. Further, residual compressive stresses have been linked to have a profound effect on mechanical properties including improved fatigue life, and improved tensile strength [37–39,114,115]. In glasses, these residual stresses have been shown to improve elongation dramatically, inducing considerable strain hardening under tensile loading [28,29]. However, it is generally accepted that the residual stresses do not play a major role in strain hardening for conventional materials since the stresses are often relaxed or balanced at the onset of plastic deformation [39]. In fact, there is evidence of this stress relaxation shown in figure

## 5.7 Conclusions

In this study, gradient structured 5005 rod was shown to exhibit both higher strength and higher total elongation to failure relative to the homogenized coarse grained control sample. The SMAT process seemed to have a similar effect for nearly all of the samples tested, independent of their gauged diameter or processing time. Although much of the literature on gradient structures derives mechanisms based on the interaction between nanocrystalline and coarse grained regions, the surprising tensile plasticity in these samples occurs in the absence of any nanocrystalline grains [24,34,54,116]. Therefore, strengthening mechanisms beyond the current theories must be developed to explain this phenomenon. One possibility is that the residual compressive stresses are relieved under tension, which could cause non-uniform deformation to occur within the gradient, though this mechanism has not been formally used to explain gradient structure mechanics [30,33,35].

Because the grain size is relatively large in these samples relative to most of the gradient structure literature, it is expected that the mechanisms governing mechanical mismatches between hard surface layers and soft interior layers will be reduced. Therefore, the magnitude of the residual stress strengthening will be enhanced, which could be the major source of strengthening in these samples. XRD showed high residual stresses at the surface, and a reduction in GND density and microhardness testing were both found at strains of 0.8%. This reduction could be the result of the relaxation of surface residual compressive stresses and would support evidence given in previous studies [28–30,117]. However, the GND density evolution and asymmetric hardening along the gradient also point to complex

mechanisms above yielding that are not clear at this point. Future studies should utilize XRD or high resolution EBSD to map the residual stress state evolution during tensile testing to determine its effect on strengthening within gradients. Further, a comprehensive Finite Element Modeling study should include the effects of multiaxial stresses and their evolution during tensile testing to conclusively identify strengthening mechanisms in gradient structured metals.

## 6 Conclusions and Future Work

Although the study of gradient structure deformation mechanisms has only recently begun, there are strong indications that the interplay between ultra-hard and ultra-ductile regions within the gradient can lead to outstanding structural performance. In this work, several previously unreported phenomenon were observed in gradient structures synthesized by SMAT. At the surface, the shear strain was calculated to exceed 100, which is among some of the highest shear strains reported in the SPD literature. In addition, it was discovered that a strong texture gradient develops in conjunction with the well-known grain size gradient. Interestingly, this texture gradient was completely different for round and flat samples, as the round samples exhibited crystallographic features indicating that shearing was occurring radially across the gauged section. Although the strengthening effect of this texture has not been quantified, the graded round samples did exhibit strengthening higher than predicted relative to the mild improvement in hardness at the surface. Some of this strengthening has to come from multiaxial stresses developing within the gradient, and experimental evidence of this was observed via the early stage wire texture development normal to the tensile axis. Another phenomenon that should contribute to the unexpected results is the accumulation of residual stresses within the gradient due to the SMAT process itself. The magnitude of the residual compression in the 5005 rod was higher than the o-tempered yield strength, and should significantly contribute to enhanced strength. Evidence for this strengthening was found via reduction in hardness and GND density at low strains. Above the yield strength, the hardness and GND density evolution was complex, and would

not be accounted for by residual stresses. Given the drop in GND density evolution along the gradient of SMATed 5005 aluminum rod, and in the absence of any obvious grain growth at various tensile strain, two of the prevailing theories do not appear to account for the strengthening observed in these samples. Therefore more studies focusing on the role of residual stresses in gradient structures must be conducted to elucidate this effect.

Considering the rapid development and bright future ahead of high resolution strain analysis using EBSD, many unanswered questions about deformation mechanisms in the field of gradient structures should be nearly obtainable. Although XRD and neutron diffraction techniques are immediately available to quantify the stress state evolution, GND activity, and grain coarsening mechanisms that are core to current theories on deformation mechanics, the wealth of information available in EBSD data sets and relative speed of acquisition surely gives it an advantage for future investigations. Future studies should rigorously investigate the mechanics governing stress state evolution, texture development, grain growth, microhardness evolution and other variables intrinsically linked to the microstructure and mechanical properties. With more robust studies exploring these effects, metallurgists will have a better understanding of how to incorporate these extraordinary materials into society.

## 7 REFERENCES

- [1] H. Gleiter, *Adv. Mater.* 4 (1992) 474–481.
- [2] E.O. Hall, *Proc. Phys. Soc. Sect. B* 64 (1951) 747–753.
- [3] N.J. Petch, *Prog. Met. Phys.* 5 (1954) 1–52.
- [4] K. Kumar, H. Van Swygenhoven, S. Suresh, *Acta Mater.* 51 (2003) 5743–5774.
- [5] H. Gleiter, *Acta Mater.* 48 (2000) 1–29.
- [6] R.Z. Valiev, I.V. Alexandrov, Y.T. Zhu, T.C. Lowe, *J. Mater. Res.* 17 (2002) 5–8.
- [7] Y. Wang, M. Chen, F. Zhou, E. Ma, *Nature* 419 (2002) 912–915.
- [8] R.Z. Valiev, *Met. Mater. Int.* 7 (2001) 413–420.
- [9] R. Valiev, *Nat. Mater.* 3 (2004) 511–516.
- [10] K. Lu, J. Lu, *Mater. Sci. Eng. A* 375–377 (2004) 38–45.
- [11] X. Wu, N. Tao, Y. Hong, G. Liu, B. Xu, J. Lu, K. Lu, *Acta Mater.* 53 (2005) 681–691.
- [12] K. Wang, N.R. Tao, G. Liu, J. Lu, K. Lu, *Acta Mater.* 54 (2006) 5281–5291.
- [13] L. Zhou, G. Liu, X.L. Ma, K. Lu, *Acta Mater.* 56 (2008) 78–87.
- [14] T.H. Fang, W.L. Li, N.R. Tao, K. Lu, *Science* 331 (2011) 1587–1590.
- [15] X.L. Wu, P. Jiang, L. Chen, J.F. Zhang, F.P. Yuan, Y.T. Zhu, *Mater. Res. Lett.* 2 (2014) 185–191.
- [16] X. Wu, P. Jiang, L. Chen, F. Yuan, Y.T. Zhu, *Proc. Natl. Acad. Sci.* 111 (2014) 7197–7201.
- [17] S. Suresh, *Science* 292 (2001) 2447–2451.
- [18] X. Wu, M. Yang, F. Yuan, G. Wu, Y. Wei, X. Huang, Y. Zhu, *Proc. Natl. Acad. Sci.* 112 (2015) 14501–14505.
- [19] X. Yang, X. Ma, J. Moering, H. Zhou, W. Wang, Y. Gong, J. Tao, Y. Zhu, X. Zhu, *Mater. Sci. Eng. A* 645 (2015) 280–285.
- [20] H. Murdoch, K. Darling, A. Roberts, L. Kecskes, *Metals* 5 (2015) 976–985.
- [21] K. Lu, *Science* 345 (2014) 1455–1456.
- [22] T.H. Fang, N.R. Tao, K. Lu, *Scr. Mater.* 77 (2014) 17–20.
- [23] L.J. Ebert, S.S. Hecker, C.H. Hamilton, *J. Compos. Mater.* 2 (1968) 458–476.
- [24] Z. Zeng, X. Li, D. Xu, L. Lu, H. Gao, T. Zhu, *Extreme Mech. Lett.* (2015).
- [25] T.J. Rupert, D.S. Gianola, Y. Gan, K.J. Hemker, *Science* 326 (2009) 1686–1690.
- [26] D.S. Gianola, S. Van Petegem, M. Legros, S. Brandstetter, H. Van Swygenhoven, K.J. Hemker, *Acta Mater.* 54 (2006) 2253–2263.
- [27] M. Legros, D.S. Gianola, K.J. Hemker, *Acta Mater.* 56 (2008) 3380–3393.
- [28] Y. Zhang, W.H. Wang, A.L. Greer, *Nat. Mater.* 5 (2006) 857–860.
- [29] X.L. Lu, Q.H. Lu, Y. Li, L. Lu, *Sci. Rep.* 3 (2013).
- [30] J.W. Tian, K. Dai, J.C. Villegas, L. Shaw, P.K. Liaw, D.L. Klarstrom, A.L. Ortiz, *Mater. Sci. Eng. A* 493 (2008) 176–183.
- [31] A.L. Ortiz, J.W. Tian, J.C. Villegas, L.L. Shaw, P.K. Liaw, *Acta Mater.* 56 (2008) 413–426.
- [32] J.C. Villegas, L.L. Shaw, *Acta Mater.* 57 (2009) 5782–5795.
- [33] M. Ya, Y. Xing, F. Dai, K. Lu, J. Lu, *Surf. Coat. Technol.* 168 (2003) 148–155.

- [34] H.W. Huang, Z.B. Wang, J. Lu, K. Lu, *Acta Mater.* 87 (2015) 150–160.
- [35] S. Wang, Y. Li, M. Yao, R. Wang, *J. Mater. Process. Technol.* 73 (1998) 64–73.
- [36] X. Zhou, F. Belahcene, F. Thomas, J. Lu, in: , 2006.
- [37] M. Torres, *Int. J. Fatigue* 24 (2002) 877–886.
- [38] P.J. Withers, H.K.D.H. Bhadeshia, *Mater. Sci. Technol.* 17 (2001) 355–365.
- [39] P.J. Withers, H.K.D.H. Bhadeshia, *Mater. Sci. Technol.* 17 (2001) 366–375.
- [40] U.F. Kocks, C.N. Tomé, H.-R. Wenk, eds., *Texture and Anisotropy: Preferred Orientations in Polycrystals and Their Effect on Materials Properties*, Cambridge Univ. Press, Cambridge, 1998.
- [41] A.B. Lopes, F. Barlat, J.J. Gracio, J.F. Ferreira Duarte, E.F. Rauch, *Int. J. Plast.* 19 (2003) 1–22.
- [42] T.L. Richard, R.T. Derricott, *J. Appl. Crystallogr.* 3 (1970) 234–242.
- [43] K. Inal, P.D. Wu, K.W. Neale, *Int. J. Plast.* 16 (2000) 635–648.
- [44] G.I. Taylor, *Proc. R. Soc. Lond. Ser. Math. Phys. Sci.* 168 (1938) 302–317.
- [45] D.P. Field, T.W. Nelson, Y. Hovanski, K.V. Jata, *Metall. Mater. Trans. A* 32 (2001) 2869–2877.
- [46] H.J. Bunge, *Krist. Tech.* 5 (1970) 145–175.
- [47] G.R. Canova, U.F. Kocks, J.J. Jonas, *Acta Metall.* 32 (1984) 211–226.
- [48] J. Nye, *Acta Metall.* 1 (1953) 153–162.
- [49] E. Kroner, *Z. Phys.* 142 (1955) 463–475.
- [50] M.F. Ashby, *Philos. Mag.* 21 (1970) 399–424.
- [51] H. Gao, *J. Mech. Phys. Solids* 47 (1999) 1239–1263.
- [52] Y. Samih, B. Beausir, B. Bolle, T. Grosdidier, *Mater. Charact.* 83 (2013) 129–138.
- [53] X. Wu, M. Yang, F. Yuan, G. Wu, Y. Wei, X. Huang, Y. Zhu, *Proc. Natl. Acad. Sci.* 112 (2015) 14501–14505.
- [54] Y. Shen, C. Wen, X. Yang, Y. Pang, L. Sun, J. Tao, Y. Gong, X. Zhu, *J. Mater. Eng. Perform.* 24 (2015) 5058–5064.
- [55] A.J. Wilkinson, T.B. Britton, J. Jiang, P.S. Karamched, *IOP Conf. Ser. Mater. Sci. Eng.* 55 (2014) 012020.
- [56] S.I. Wright, M.M. Nowell, D.P. Field, *Microsc. Microanal.* 17 (2011) 316–329.
- [57] J. Kacher, C. Landon, B.L. Adams, D. Fullwood, *Ultramicroscopy* 109 (2009) 1148–1156.
- [58] D. Fullwood, M. Vaudin, C. Daniels, T. Ruggles, S.I. Wright, *Mater. Charact.* 107 (2015) 270–277.
- [59] Q. Wei, K.T. Ramesh, L.J. Kecskes, S.N. Mathaudhu, K.T. Hartwig, *Mater. Sci. Forum* 579 (2008) 75–90.
- [60] X.Z. Liao, A.R. Kilmametov, R.Z. Valiev, H. Gao, X. Li, A.K. Mukherjee, J.F. Bingert, Y.T. Zhu, *Appl. Phys. Lett.* 88 (2006) 021909.
- [61] E.A. El-Danaf, *Mater. Sci. Eng. A* 487 (2008) 189–200.
- [62] W.Y. Chen, W.P. Tong, C.S. He, X. Zhao, L. Zuo, *Mater. Sci. Forum* 706-709 (2012) 2663–2667.

- [63] R. Blonde, H.-L. Chan, N. Allain-Bonasso, B. Bolle, T. Grosdidier, J. Lu, *J. Alloys Compd.* 504 (2010) S410–S413.
- [64] H. Zhang, Z. Hei, G. Liu, J. Lu, K. Lu, *Acta Mater.* 51 (2003) 1871–1881.
- [65] N.R. Tao, Z.B. Wang, W.P. Tong, M.L. Sui, J. Lu, K. Lu, *Acta Mater.* 50 (2002) 4603–4616.
- [66] K.A. Darling, M.A. Tschopp, A.J. Roberts, J.P. Ligda, L.J. Kecskes, *Scr. Mater.* 69 (2013) 461–464.
- [67] J.W. Tian, K. Dai, J.C. Villegas, L. Shaw, P.K. Liaw, D.L. Klarstrom, A.L. Ortiz, *Mater. Sci. Eng. A* 493 (2008) 176–183.
- [68] K. Dai, J. Villegas, Z. Stone, L. Shaw, *Acta Mater.* 52 (2004) 5771–5782.
- [69] A.J. Wilkinson, T.B. Britton, *Mater. Today* 15 (2012) 366–376.
- [70] T. Benjamin Britton, A.J. Wilkinson, *Acta Mater.* 60 (2012) 5773–5782.
- [71] A.J. Wilkinson, G. Meaden, D.J. Dingley, *Ultramicroscopy* 106 (2006) 307–313.
- [72] T.B. Britton, A.J. Wilkinson, *Ultramicroscopy* 111 (2011) 1395–1404.
- [73] E. Plancher, J. Petit, C. Maurice, V. Favier, L. Saintoyant, D. Loisonard, N. Rupin, J.-B. Marijon, O. Ulrich, M. Bornert, J.-S. Micha, O. Robach, O. Castelnau, *Exp. Mech.* 56 (2016) 483–492.
- [74] W. Pantleon, *Scr. Mater.* 58 (2008) 994–997.
- [75] S.I. Wright, D.P. Field, M.M. Nowell, *Mater. Sci. Forum* 495-497 (2005) 1121–1130.
- [76] J. Jiang, T.B. Britton, A.J. Wilkinson, *Acta Mater.* 61 (2013) 7227–7239.
- [77] J.C. Villegas, L.L. Shaw, *Acta Mater.* 57 (2009) 5782–5795.
- [78] K. Dai, L. Shaw, *Mater. Sci. Eng. A* 463 (2007) 46–53.
- [79] Y. Ivanisenko, W. Lojkowski, R.Z. Valiev, H.-J. Fecht, *Acta Mater.* 51 (2003) 5555–5570.
- [80] A. Ramesh, S.N. Melkote, L.F. Allard, L. Riestler, T.R. Watkins, *Mater. Sci. Eng. A* 390 (2005) 88–97.
- [81] S.V.S.N. Murty, S. Torizuka, K. Nagai, *Mater. Trans.* 46 (2005) 2454–2460.
- [82] N. Kamikawa, T. Sakai, N. Tsuji, *Acta Mater.* 55 (2007) 5873–5888.
- [83] Q. Wei, K.T. Ramesh, L.J. Kecskes, S.N. Mathaudhu, K.T. Hartwig, *Mater. Sci. Forum* 579 (2008) 75–90.
- [84] S. Shekhar, S. Abolghasem, S. Basu, J. Cai, M.R. Shankar, *J. Manuf. Sci. Eng.* 134 (2012) 031008.
- [85] N. Kamikawa, T. Sakai, N. Tsuji, *Acta Mater.* 55 (2007) 5873–5888.
- [86] J. Moering, X. Ma, G. Chen, P. Miao, G. Li, G. Qian, S. Mathaudhu, Y. Zhu, *Scr. Mater.* 108 (2015) 100–103.
- [87] G. Langford, *Metall. Trans. A* 8 (1977) 861–875.
- [88] D. Li, H.N. Chen, H. Xu, *Appl. Surf. Sci.* 255 (2009) 3811–3816.
- [89] W.Y. Chen, W.P. Tong, C.S. He, X. Zhao, L. Zuo, *Mater. Sci. Forum* 706-709 (2012) 2663–2667.
- [90] K. Lu, J. Lu, *Mater. Sci. Eng. A* 375-377 (2004) 38–45.
- [91] H.W. Huang, Z.B. Wang, J. Lu, K. Lu, *Acta Mater.* 87 (2015) 150–160.
- [92] Y.S. Zhang, Z. Han, K. Wang, K. Lu, *Wear* 260 (2006) 942–948.

- [93] Y. Todaka, M. Umemoto, K. Tsuchiya, *Mater. Trans.* 45 (2004) 376–379.
- [94] H. Kitahara, T. Yada, F. Hashiguchi, M. Tsushida, S. Ando, *Surf. Coat. Technol.* 243 (2014) 28–33.
- [95] J.L. Liu, M. Umemoto, Y. Todaka, K. Tsuchiya, *J. Mater. Sci.* 42 (2007) 7716–7720.
- [96] H.W. Höppel, J. May, M. Göken, *Adv. Eng. Mater.* 6 (2004) 219–222.
- [97] D. Tabor, *Rev. Phys. Technol.* 1 (1970) 145–179.
- [98] S.C. Chang, M.T. Jahn, C.M. Wan, J.Y.M. Lee, T.K. Hsu, *J. Mater. Sci.* 11 (1976) 623–630.
- [99] J.R. Cahoon, W.H. Broughton, A.R. Kutzak, *Metall. Trans. A* 2 (1971) 1979–1983.
- [100] H. Kuhn, D. Medlin, *Hardness and Tensile Properties*, 2000.
- [101] E.R. Petty, *Metallurgia* 63 (1962) 25–26.
- [102] N. Rangaraju, T. Raghuram, B.V. Krishna, K.P. Rao, P. Venugopal, *Mater. Sci. Eng. A* 398 (2005) 246–251.
- [103] E.A. El-Danaf, *Mater. Sci. Eng. A* 487 (2008) 189–200.
- [104] Y. Kwon, *Scr. Mater.* 49 (2003) 785–789.
- [105] M. Eizadjou, H.D. Manesh, K. Janghorban, *J. Alloys Compd.* 474 (2009) 406–415.
- [106] C. Xu, Z. Horita, T.G. Langdon, *Mater. Trans.* 51 (2010) 2–7.
- [107] D.V. Wilson, P.S. Bate, *Acta Metall. Mater.* 42 (1994) 1099–1111.
- [108] T. Roland, D. Retraint, K. Lu, J. Lu, *Scr. Mater.* 54 (2006) 1949–1954.
- [109] J. Li, A.K. Soh, *Int. J. Plast.* 39 (2012) 88–102.
- [110] R. Lapovok, P.W.J. McKenzie, P.F. Thomson, S.L. Semiatin, *J. Mater. Sci.* 42 (2007) 1649–1659.
- [111] N. Allain-Bonasso, F. Wagner, S. Berbenni, D.P. Field, *Mater. Sci. Eng. A* 548 (2012) 56–63.
- [112] U. Welzel, J. Ligot, P. Lamparter, A.C. Vermeulen, E.J. Mittemeijer, *J. Appl. Crystallogr.* 38 (2005) 1–29.
- [113] T.R. Simes, S.G. Mellor, D.A. Hills, *J. Strain Anal. Eng. Des.* 19 (1984) 135–137.
- [114] A. Azhari, C. Schindler, B. Li, *Int. J. Adv. Manuf. Technol.* 67 (2013) 785–795.
- [115] P.B. Trivedi, R.S. Yassar, D.P. Field, R. Alldredge, *Mater. Sci. Eng. A* 425 (2006) 205–212.
- [116] N. Guo, B. Song, H. Yu, R. Xin, B. Wang, T. Liu, *Mater. Des.* 90 (2016) 545–550.
- [117] X. Chen, J. Yan, A.M. Karlsson, *Mater. Sci. Eng. A* 416 (2006) 139–149.